Improving fatigue life for additively manufactured AlSi10Mg

Sebastian Levin[1] and Jendrik-Alexander Tröger[2] and Hagen Lukas Kock[1] and Colin Dommes[1] and Andreas Krevet[3] and Stefan Hartmann[2] and Uwe Wolfram[1,*]

[1]*Institute of Materials Science and Engineering, Clausthal University of Technology, Clausthal-Zellerfeld, Germany*

[2]*Division of Solid Mechanics, Institute of Applied Mechanics, Clausthal University of Technology, Germany*

[3]*Department of New Technologies, Production Planning, Volkswagen AG*

Abstract

While laser powder bed fusion enables rapid and resource-efficient production, challenges such as microstructural defects, porosity, and unfavourable residual stresses compromise the durability of components under dynamic loading. Thus, we investigated methods to enhance fatigue life of AlSi10Mg produced by laser powder bed fusion. To do so, we explore the effects of manual polishing, heat treatment, and deep rolling on the mechanical properties and fatigue performance of AlSi10Mg.

Specimens were fabricated and divided into five groups: as-built, as-built with manual polishing, heat-treated and manually polished, as-built with deep rolling, and heat-treated with deep rolling. These groups underwent surface roughness measurements, residual stress analysis, hardness testing, and microscopy. The primary evaluation of fatigue performance was conducted using a rotating bending test rig under a load ratio of R = -1, following the high-cycle fatigue string-of-pearl method.

The fatigue tests revealed significant differences among the treatment groups. The as-built specimens exhibited the lowest fatigue life, with cracks initiating from surface defects. While polishing and heat treatment provided moderate improvements, specimens treated with deep rolling exhibited the highest bearable stress amplitudes and the flattest S–N curves, indicating a significant improvement in fatigue resistance. The slope of the S–N curve in this condition is 7.8 times flatter compared to the untreated as-built condition. At a defined number of load cycles of 1E+06, the bearable stress in the "as-built + deep rolling" condition reaches 251 MPa, which is ~8.5 times the stress amplitude tolerated in the untreated as-built condition. Interestingly, combining heat treatment with deep rolling resulted in a decrease in performance compared to deep rolling alone.

Our results indicate that surface treatment is critical for improving the fatigue life of additively manufactured AlSi10Mg components. It has turned out that deep rolling is an effective and economical method, as it reduces surface roughness and induces beneficial compressive residual stresses that counteract crack initiation. Furthermore, deep rolling eliminates the need for subsequent heat treatment, which may even be counter-productive, thus saving both time and energy costs. Our results help to exploit the potential of laser powder bed fusion of AlSi10Mg by combining near-net-shape production with effective surface enhancement.

Keywords: Laser powder bed fusion; fatigue testing; surface treatment; heat treatment; deep rolling; residual stress; parameter identification

* Correspondence to uwe.wolfram@tu-clausthal.de

1 Introduction

Laser powder bed fusion (LPBF) of aluminium alloys enables rapid and cost-efficient production of complex geometries, thereby shortening development times and facilitating product variability [1,2]. Particularly in the area of chassis components, such as wheel suspensions or steering knuckles, LPBF enables production of complex geometries without the need for conventional casting moulds. In this context, AlSi10Mg is gaining increasing importance due to its good castability, mechanical properties, and corrosion resistance. Remarkably, the mechanical properties are reported to exceed even those of die cast alloys of similar composition [3]. However, ensuring material durability and improving the mechanical properties of additively manufactured components remains a challenge, especially for components subjected to dynamic loading.

However, using AlSiMg alloys faces several challenges. One major issue is the formation of microstructural defects, such as porosity and cracks, during the layer-by-layer fabrication process. These defects arise from the rapid cooling rates and thermal gradients inherent in additive manufacturing (AM) techniques [4,5]. Corrosion resistance is another concern, as the fine microstructure of LPBF-produced AlSiMg alloys can lead to localised corrosion under certain environmental conditions. Consequently, optimising alloy composition and surface treatments is essential to mitigate these issues [5,6].

Surface strengthening techniques such as shot peening and deep rolling are employed to improve the durability and mechanical properties of additively manufactured components [7–12]. These post-processing steps are essential, as components produced by the powder bed process often exhibit higher porosity and different microstructures compared to conventionally cast parts [13,14]. Furthermore, additively manufactured AlSiMg alloys exhibit anisotropic mechanical properties due to directional solidification during printing. This anisotropy can compromise the structural integrity of components under dynamic loading conditions [15,16]. Consequently, achieving consistent material properties across different build orientations remains difficult, requiring targeted post-processing steps like heat treatment, shot peening, or deep rolling [17,18] that takes build orientations into account [19].

Functional prototypes from AlSi10Mg using LPBF can be produced on a Concept Laser X Line system with a build volume of 800 × 400 × 500 mm [20,21]. These prototypes enable real-world load testing during early development phases without the need to manufacture elaborate casting moulds. To do so, component geometries are typically designed with casting in mind to facilitate a transition to series production using aluminium die casting later on.

Generally, LPBF promises cost-effective production of small quantities with large variation. Digitalisation of the manufacturing process allows minimization of waste, which in turn translates into reduced costs and enhanced resource conservation [22,23]. This, however, requires data close to the intended use. In the automotive industry, dynamic loading scenarios and fatigue loading are essential. However, there appears to be a gap with regard to such properties in the context of LPBF-produced AlSi10Mg.

Previous investigations have highlighted the effects of shot peening, polishing, heat treatments, and deep rolling on durability and mechanical properties. Despite its advances, particular challenges remain in improving material durability and dynamic behaviour of LPBF-produced AlSi10Mg. Therefore, this study aims to explore pathways to enhance the fatigue lifetime of additively manufactured AlSi10Mg through surface treatment methods, contributing to resource-efficient manufacturing

practices. Our specific objectives are to explore (i) deep rolling for surface treatment; (ii) polishing; (iii) heat treatments; and (iv) conduct rotation-bending tests to assess lifetime improvements through methods (i-iii).

2 Materials and Methods

In the following, the different specimen conditions, their preparation, and the testing methodology are described. The specimen preparation is explained in Section 2.1, where the five different conditions are introduced that we investigate in this work. The deep rolling process is covered in Section 2.2. Afterwards, the roughness testing (Section 2.3), the residual stress analysis (Section 2.4), and the hardness testing and microscopy (Section 2.5) are described. The fatigue testing as core part of this study is briefly explained in Section 2.6, followed by the setting for the quasi-static tensile experiments (Section 2.7).

2.1 Specimen preparation

The chosen AlSi10Mg alloy is a heat-treatable and hardenable cast alloy (ASTM F3318), which is primarily used in the automotive and aerospace industries [24]. It consists of up to 10% silicon and a maximum of 0.5% magnesium as alloy elements. The magnesium content enhances corrosion resistance and promotes precipitation hardening when subjected to appropriate heat treatment. Furthermore, near eutectic Al-Si alloys such as AlSi10Mg exhibit a narrow solidification range, low thermal expansion, and high melt pool flowability, which contribute to low shrinkage and a significantly reduced susceptibility to hot cracking during processing. These excellent casting and machining properties also make this alloy highly suitable for the Laser Powder Bed Fusion (L-PBF) process [19].

Fifty-three waisted dumbbell-shaped specimens were fabricated, featuring a waist radius of 30 mm, a reduced central section of 9 mm diameter and shoulders of 12 mm diameter for clamping (Figure 1 and A1). We chose this specimen geometry as it has a stress concentration factor $K_T > 1$, leads to locally confined stress states, and reduces time-dependent deformation effects. The resulting stress gradient should minimise the influence of creep effects, which can be observed in cylindrical, unnotched specimens under loads near the yield strength (DIN 50100). This strategy enables a reliable analysis of the finite life fatigue regime across various material states in the fatigue test.

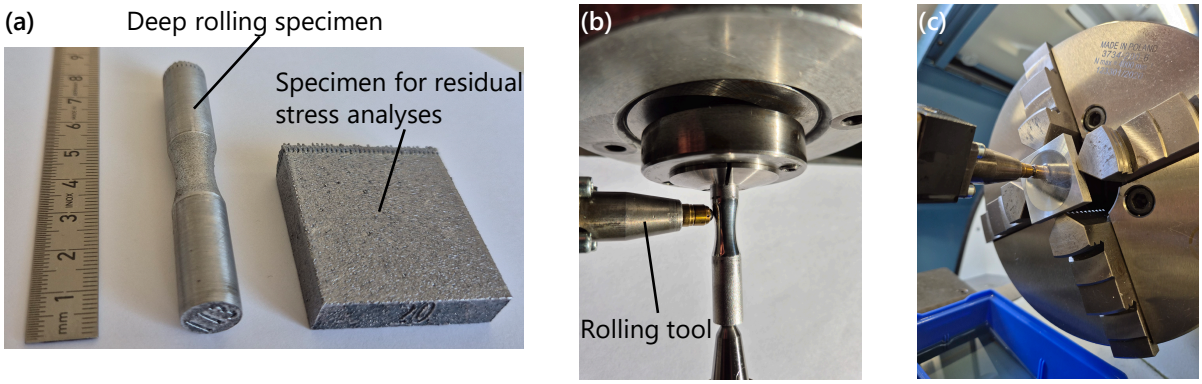

Figure 1 – Specimens for deep rolling and residual stress analyses. *(a) Exemplary specimens for fatigue and hardness testing. See also Figure A1 for the dimensions of the deep rolling specimen. (b) Deep rolling setup in a lathe. On the left, the tip of the deep rolling tool is visible and in contact with the process zone surface of the fatigue testing specimen. (c) Deep rolling of the specimen for residual stress analyses.*

We manufactured specimens on an industrial laser powder bed fusion system (X Line 2000R, Concept Laser) with a dual-laser architecture (2 × 1 kW) operating under a protective gas atmosphere (argon

or nitrogen). We preheated the build platform to 100 °C to minimise thermal stresses. For the specimens investigated here, we used the manufacturer's productivity parameter (Parameter 395). This parameter is characterised by a 50 µm layer thickness, nitrogen as the process gas, and a typical build rate of 50.9 cm^3/h. According to the material datasheet, the mechanical properties in the stress-relieved annealed condition are: tensile strength up to 300 MPa, elongation up to 13.5%, and hardness of approximately 89 HV5. The upskin surface roughness is about 10–13 µm, which necessitates post-processing. For comparison, the alternative surface parameter 396 uses a finer 40 µm layer thickness, argon gas, and a reduced build rate of 26.5 cm^3/h, but provides markedly improved surface quality (upskin roughness approximately 6–7 µm).

The manufactured specimens were separated into five groups (Table 1). The first group was not modified after preparation and used as-built (AB). The second group consisted of AB samples that received short, light-touch manual polishing on a lathe with silicone carbide paper (P320 grid size) to reduce surface roughness (ABMP). In the third group, ABMP specimens were heat-treated in a muffle furnace at 325 °C for two hours and subsequently cooled in still air for stress relief (HTMP). The fourth group comprises AB samples whose surfaces were modified by deep rolling (ABDR) (Figures 1 and A1, Section 2.2). The specimens of the fifth group were also subjected to stress-relief annealing prior to deep rolling (HTDR). The latter group served only for comparison with the ABDR.

Table 1 – Conditions of AlSi10Mg specimens.

Condition	Surface treatment	Heat treatment
AB	×	×
ABMP	✓ (manual polishing)	×
HTMP	✓ (manual polishing)	✓ (2 h at 325 °C)
ABDR	✓ (deep rolling)	×
HTDR	✓ (deep rolling)	✓ (2 h at 325 °C)

2.2 Roughness and hardness testing

To quantify surface roughness, we used rectangular reference specimens of the same material subjected to the same surface preparation protocols as the four groups and the cylindrical end sections of the mechanical test specimens. We measured surface roughness using a stylus roughness tester (Perthometer S8P, Mahr-Perthen) equipped with a diamond tip (RFHTB-250). Roughness was measured along a traverse length $l_T = 5.6$ mm with a cut-off length $l_C = 0.8$ mm across the surface of the samples. From these measurements, we derived average roughness depth R_z in µm as a surface characteristic. R_z allows us to additionally illustrate the effects of deep rolling and manual finishing in comparison to the AB condition, enabling us to determine whether the surface roughness promotes notch sensitivity. We tested one specimen per condition as production means were similar for all other specimens.

For hardness testing, specimens were ground with a series of silicon carbide papers (P800, P1200, P2400) (Knuth Rotor 2, Struers). This was followed by polishing for 4 minutes (RotoPol-35 with RotoForce-4, Struers) with a woven cloth and 1 µm alumina suspension at 15 N contact force. We conducted Vickers hardness testing following DIN EN ISO 6507-1 using a hardness tester (Duramin, Struers). Since the outer rim of the specimens is of interest due to the different surface modifications, we conducted hardness testing with HV0.1 (Duramin-10, Struers). To determine a hardness profile

across the cross-section, we measured hardness from the edge of the specimen cross-section towards its centre with a distance of 1 mm (Figure 1).

2.3 Microscopy

To facilitate microscopy, specimens were prepared similar to hardness testing (Section 2.3). After grinding, we etched specimens chemically using a slightly modified Kroll [25] agent with 100 ml deionised water, 5ml nitric acid, and 2 ml hydrofluoric acid for 15 s. Etching was controlled visually under a desktop microscope. We acquired microscopy images with a light microscope equipped with a CCD camera (Axiolpan 2, Zeiss). The heat-treated samples could not be successfully etched with Kroll's reagent because the precipitated silicon reacted too strongly with the etchant, resulting in no useful contrast. To facilitate microscopy on these specimens, we employed a modified sodium hydroxide etching with 3% aqueous sodium hydroxide (aq. NaOH). We immersed specimens in aq. NaOH for ~10 s with a visual check. Subsequently we immersed the specimens in 5% aqueous nitric acid for 5 s. Thereafter, we rinsed the specimens with running water for 3 min and shortly with ethanol. Finally, we dried the specimens in a warm air stream.

2.4 Deep rolling

Because we used the productivity parameter 395, surface post-processing was required to prepare the parts for dynamic loading tests. We employ deep rolling as a proven and widely available surface finishing technique [26] with a deep rolling tool (Ecoroll AG) on a classic lathe (Matador, Weiler). The aim was to enhance the fatigue life under realistic operating conditions by reducing surface roughness and influencing residual stresses. The fundamental principle involves pressing a roller or ball with a force F against the surface to be rolled while it rotates (Figure 1). Partial plastic deformation induces compressive residual stresses, which should counteract crack growth under load. The rolling action creates cold hardening in the surface layers, stabilising the compressive residual stresses and increasing the resistance to crack initiation. Another benefit is the smoothing of the surface as roughness is flattened. Additionally, deep rolling mitigates notch effects and, therefore, may contribute to higher strengths. The samples were prepared with hand finishing and subsequently rolled on a lathe under a pressure of 100 bar, which ultimately resulted in a contact force of 251 N.

2.5 Residual stress analyses

The borehole method was utilised for residual stress analyses [27], employing a bespoke testing rig with a pneumatic driller (MTU Aero Engines). To facilitate this, separate hexahedral specimens were produced following the same preparation protocols. Our drilling cycle involved creating a circular pocket, which was accomplished by implementing a systematic drilling procedure. We stopped at each drilling stage to ensure temperature equalisation, to enhance the accuracy of our measurements. For this process, we used a tungsten carbide drill with a diameter of 1.6 mm to produce a pocket diameter of 1.8 mm. A drilling depth of 1.2 mm was achieved, with a specific determination depth of 1.01 mm. The rig operated at a high rotational frequency of 160,000 rpm, enabling efficient material removal and precise machining. We positioned the data acquisition system (Micro-Measurements MMF003671), positioned on a flat sample measuring 40 × 40 × 10 mm, an example of the test is shown in Appendix 7.2. In terms of orientation, we aligned the z- and y-directions with the measured residual stresses. The z-direction corresponds to the build direction of the additive manufacturing process. We performed one measurement per condition.

2.6 Fatigue testing

We conducted fatigue testing on a rotating bending test rig (Sincotec GmbH). This is a surface sensitive method concentrating stresses into the periphery of the specimens where surface modifications due to post-processing directly impact fatigue life. The load application involves a 4-point bending configuration at a temperature of 19 - 20 °C (laboratory conditions). We used a load ratio of R = -1 with amplitude ranges σ_a in MPa (Table 2) and a rotational frequency of 44 Hz. Our testing procedure follows the evaluation of the high-cycle fatigue (HCF) range according to the string-of-pearls method outlined in DIN 50100. Amplitudes were identified iteratively in pre-liminary tests.

Table 2 – Nominal stress amplitudes σ_a *in MPa tested in each group (see Table 1, Section 2.1, for the conditions). Abbreviations denote as-built (AB), as-built + manual polishing (ABMP), as built + manual polishing + heat-treated (HTMP), as-built deep rolling (ABDR), and heat-treated + deep rolling (HTDR).*

	Nominal stress amplitudes σ_a in MPa											
AB	200.0	150.0	125.0	112.5	100.0	87.5	75.0	62.5	50.0	37.5	25.0	12.5
ABMP	150.0	140.0	130.0	120.0	110.0	100.0	90.0	80.0	70.0	60.0		
HTMP	140.0	130.0	120.0	110.0	100.0	90.0	80.0	70.0	60.0			
ABDR	300.0	280.0	270.0	260.0	250.0	240.0	230.0	160.0	120.0			
HTDR	160.0	150.0	140.0	130.0	120.0	110.0	100.0	90.0				

2.7 Quasi-static tensile testing

2.7.1 Tensile experiments

Additionally, tensile tests were performed on specimens with a dumbbell shape as illustrated in Figure 1. Of course, we are aware that the specimen shape is not ideal for achieving a homogeneous uniaxial tensile stress state, but we wanted to compare conditions quasi-statically using specimens produced in the same fashion as for fatigue testing. Since the used shape inevitably introduces shear stresses, we provide an analysis of this impact in Section 3.4.

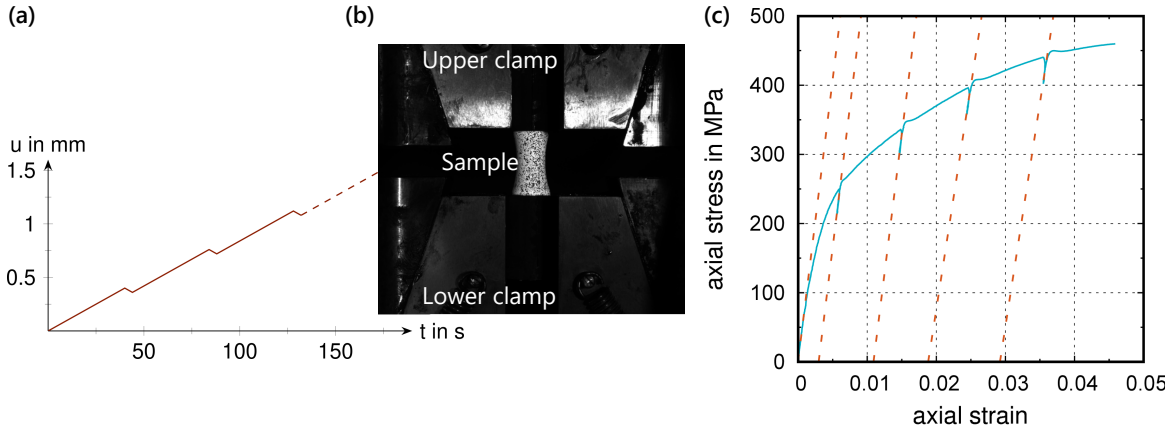

Figure 2 – Tensile testing: *(a) displacement-time curve for the conducted tensile testes. (b) an exemplary sample clamped in the tensile tester. The b/w speckle pattern for the digital image correlation is visible. (c) illustrates the determination of damage (D) by measuring the change in stiffness (red dashed lines) during partial unloading (see also Figure 9).*

We utilised a Zwick/Roell Z100 with hydraulic clamping and cylindrical steel collets (clamping pressure 100 bar). Tensile stress was calculated as axial force divided by the smallest cross-section of the specimen. We observed the surface deformation using a stereo-correlation-based digital image correlation system (ARAMIS 12M, Carl Zeiss GOM, Braunschweig) with two visible light cameras. A light projector (blue light technology) was exploited to minimise reflections and distortions from other

light sources. The image correlation was performed with ARAMIS Professional (Carl Zeiss GOM, Braunschweig) with a facet size of 15 px and a point distance of 12 px. The axial strain was determined by positioning a single facet at the top and bottom of the varnished measuring region, respectively. Then, the axial strain was computed by dividing the difference in the axial displacements by the initial distance between the two centre points of the facets.

2.7.2 Parameter identification

To identify the material parameters of an elasto-plastic constitutive model from the quasi-static tensile tests, we used the nonlinear least-squares method as deterministic approach with the objective function $\phi(\boldsymbol{\kappa}) = \frac{1}{2}\left|\left|\boldsymbol{O}\left(\hat{\boldsymbol{y}}(\boldsymbol{\kappa})\right) - \boldsymbol{d}\right|\right|^2 \rightarrow \min$. Therein, $\boldsymbol{\kappa} \in \mathbb{R}^{n_\kappa}$ are the material parameters, $\boldsymbol{O}$ is the observation operator, $\hat{\boldsymbol{y}}$ represents the model response (here, the axial stress), and $\boldsymbol{d} \in \mathbb{R}^{n_d}$ is the experimental data stored as column vector. Note that $\boldsymbol{O}$ formally extracts the data from the model response to compare with the experimental data at the same points in both space and time. The solution is obtained as $\boldsymbol{\kappa}^* = \arg\min_{\boldsymbol{\kappa}} \phi(\boldsymbol{\kappa})$. Römer et al. [28] denoted this as *reduced approach*, since it could be considered necessary to solve the model equations $\boldsymbol{F}$ (here, a nonlinear mechanical finite element simulation) to obtain $\hat{\boldsymbol{y}}$. This would lead to an equality constraint $\phi(\boldsymbol{\kappa}) = \frac{1}{2}\left|\left|\boldsymbol{O}\left(\hat{\boldsymbol{y}}(\boldsymbol{\kappa})\right) - \boldsymbol{d}\right|\right|^2 \rightarrow \min$. subject to $\boldsymbol{F}(\hat{\boldsymbol{y}}(\boldsymbol{\kappa}), \boldsymbol{\kappa}) = \boldsymbol{0}$.

We employed a rate-independent small-strain von Mises-type plasticity model with nonlinear kinematic hardening as constitutive model. The numerical treatment of the model was originally developed in Hartmann and Haupt [29]. The required material parameters are bulk modulus K, shear modulus G, yield stress $\hat{k}$, as well as hardening parameters b and c.

For the parameter identification, we prescribe Poisson's ratio $\nu = 0.33$ [30], leading to a reduced parameter set for identification, $\boldsymbol{\kappa} = \{E, \hat{k}, b, c\}^T$, wherein bulk and shear modulus were converted to Young's modulus E and Poisson's ratio ν. We determined $\boldsymbol{\kappa}^*$ using our in-house code [28,29] and gradient-based schemes for solving the minimization problem. A single 8-noded hexahedral element with boundary conditions for uniaxial tension is sufficient since we assume a homogeneous uniaxial stress state. This assumption may seem questionable in view of the dumbbell-shaped specimens and is addressed in Section 3.4.

Although the nonlinear least-squares method is deterministic, the certainty of the estimate, here the material parameters $\boldsymbol{\kappa}^*$, can be quantified as uncertainty. For that, we exploit the Jacobian $\boldsymbol{J} = \frac{d\boldsymbol{O}}{d\boldsymbol{y}}\frac{d\hat{\boldsymbol{y}}}{d\boldsymbol{\kappa}}$ as it allows to approximate the Hessian in the vicinity of the solution $\boldsymbol{\kappa}^*$, so that $\boldsymbol{H}(\boldsymbol{\kappa}^*) \approx \boldsymbol{J}^T\boldsymbol{J}$. Based one the approximated Hessian, uncertainty estimates are calculated for the individual material parameters with the asymptotic covariance matrix $\boldsymbol{C} \approx s^2\boldsymbol{H}^{-1}$, employing the asymptotic properties of the nonlinear least-squares estimator [31]. Here, s^2 is an estimate for the variance of the residuals. The material parameter uncertainties $\Delta\kappa_i = \sqrt{C_{ii}}, i = 1, \ldots, n_\kappa$, are used to state confidence intervals $\boldsymbol{\kappa}^* \pm \Delta\boldsymbol{\kappa}$.

An important aspect during parameter identification is the uniqueness of the obtained solution. This is related to the concept of *local identifiability* [28]. If neither the determinant nor any sub-determinant of the approximated Hessian vanishes, the parameters are locally unique in the vicinity of the solution $\boldsymbol{\kappa}^*$.

To obtain the experimental data vector $\boldsymbol{d}$, we interpolate the experimental stress-strain data to an equidistant grid of $n_d = 100$ strain values for each specimen. The data from unloading and loading

is neglected until the previous traverse displacement was reached again, i.e. data is like a simple monotonic tensile test. For each condition, the maximum strain during parameter identification is prescribed to the axial strain value, where the earliest fracture occurs during tensile testing within the group with the same condition.

3 Results

The results are described following the same structure as in Section 2. Accordingly, the results of roughness and hardness testing are presented first in Section 3.1. Then, we proceed with the residual stress results in Section 3.2. Afterwards, the results of the fatigue testing are reported in Section 3.3. Finally, the quasi-static tensile testing and the associated parameter identification are provided in Section 3.4.

3.1 Roughness and hardness testing

The average roughness R in µm was highest in the case of AB specimens ($R_Z = 21.21$ µm) and lowest in the deep rolled specimens ($R_Z = 0.57$ µm). Manual polishing reduced surface roughness but produced slightly different values, e.g. $R_Z = 6.24$ µm and $R_Z = 8.07$ µm for two runs.
We observed the lowest hardness in heat-treated specimens. In contrast, the hardness was increased in the periphery only for deep rolled specimens ($p < 10^{-8}$, $r^2 = 0.68$) (Figure 3). The other conditions did not show such a dependence. Deep rolling influenced the surface up to a depth of 0.8 mm.

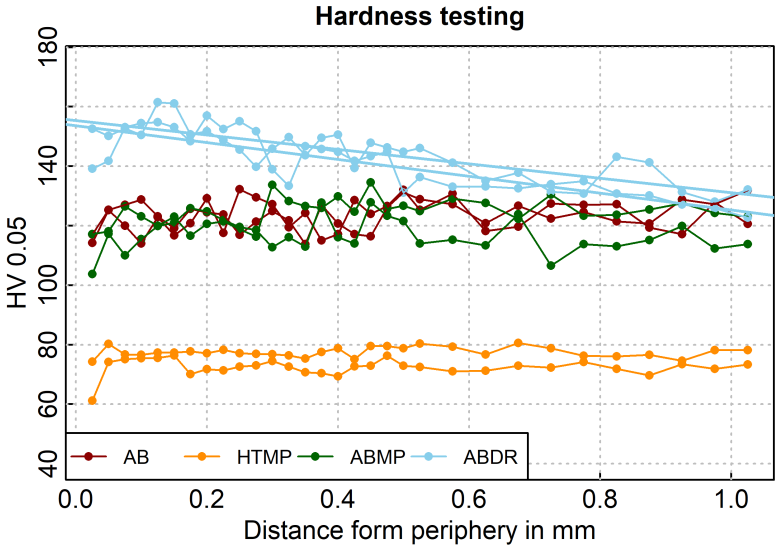

Figure 3 – Hardness testing results for exemplary specimens. *Tested groups were as-built (AB), as-built + manual polishing (ABMP), heat-treated + manual polishing (HTMP), and as-built deep rolling (ABDR). The correlation between hardness and position from periphery in case of ABDR is significant ($p < 10^{-8}$, $r^2 = 0.68$). Regression lines are only shown for significant linear regressions.*

3.2 Microscopy

Metallographic preparation reveals clear differences between the powder-bed additively manufactured as-built (AB) condition and specimens heat-treated by stress-relief annealing at 325 °C (HTMP). In the AB condition, print paths are clearly recognisable across the periphery and the centre (Figure 4) and appear as lamellar features with alternating orientation, reflecting the typical LPBF scanning strategy: the system first exposes the component contour to form an edge region, then fills the interior with parallel hatch lines. Individual print paths measure about 100–150 µm in width, consistent with the laser spot diameter and hatch spacing, while the bright contour-produced edge region is approximately 0.4 mm wide.

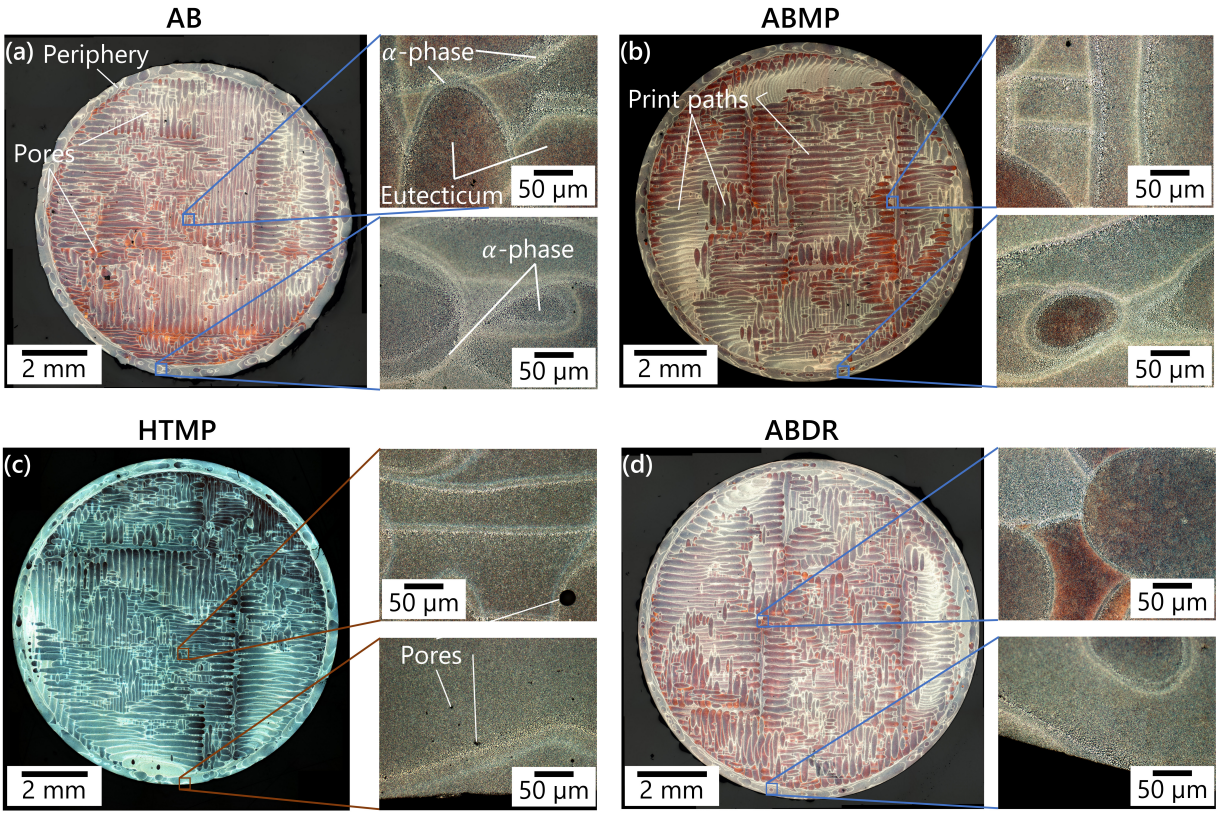

Figure 4 – Metallographic images. *The figure shows microscopy mosaics and magnifications of exemplary samples from (a) as built (AB), (b) as built and manual polishing (ABMP), (c) as built and heat treatment (HTMP), as well as (d) as built and deep rolling (ABDR). Higher magnification images of the inlay zones are shown in Appendix 7.3 (Figures A4-A6). Within the print paths (a, b, d), dark regions dominate and indicate a silicon-rich eutectic network, whereas bright rims at the print path boundaries and at the outer specimen edge point to primary α-aluminium. This microstructural distribution arises from differing cooling conditions. The periphery and the boundary zones of the print paths cool particularly rapidly, which promotes the formation of globular α-aluminium and retains part of the silicon in solution. By contrast, slower cooling in the print paths centres favours the development of a pronounced eutectic network. The difference of the HTMP specimens (c), which was etched with NaOH (Section 2.4) is striking. The fine cellular structure of α-Al with eutectic silicon breaks down due heat treatment, leading to coarsened Si particles precipitated as well as Mg_2Si [32,33].*

The periphery shows a fine-grained ring comprising globular and dendritic grains (Figure 4; Figures A4–A6 in Appendix 7.3). The boundaries of the melt tracks consist of a fine cellular α-Al structure, with eutectic silicon forming a very narrow network around the α-Al. During etching, the α-Al phase is attacked less aggressively, so these areas appear bright due to the lower contrast. Print-path boundaries consist of a fine cellular α-Al structure, with eutectic Si forming a network-like bright boundary. The interiors of the paths contain grains with fine lamellar features indicative of an eutectic condition. There is no discernible difference between AB, ABMP and ABDR (Figure 4a–c). By contrast, heat treatment (HTMP) modifies the eutectic morphology: the Si network at the print-path boundaries spheroidises, and the lamellar features within the path interiors become more finely dispersed (Figure 4; Figures A4–A6).

3.3 Residual stresses

Hole-drilling measurements in as-built AlSi10Mg show tensile residual stresses that are strongest in the build direction (z) (Figure A2). At the surface, values exceed 200 MPa (up to 230 MPa) and persist to a depth of about 0.4 mm, which corresponds to the α-Al-rich surface layer. Even at 1.0 mm depth, the maximum evaluated, stresses remain above 100 MPa. In the scan direction (y), tensile residual stresses are lower, reaching about 50 MPa down to 0.4 mm before approaching a neutral level.

Stress-relief annealing (HTMP) reduced the previously detected high tensile residual stresses in ABMP to nearly fully relieved. The as-built surface forms a complex edge zone with local inhomogeneities. Figure A2 shows a narrow tensile-stress peak at a depth of about 0.1 mm in the immediate edge region. Deep rolling (ABDR) converted the initial tensile residual stresses into compressive residual stresses. The resulting stress field is anisotropic: in the build direction (z) the compressive stress reaches about −350 MPa, while in the y-direction it is about −240 MPa. Even after stress-relief annealing, subsequent deep rolling (HTDR) can induce a pronounced compressive residual stress profile. However, the achievable compressive stresses, particularly in the immediate surface region, are lower because the heat treatment reduces the base strength of the material (Figure A2).

3.4 Fatigue testing

The AB specimens featured the steepest negative slope of the S-N curve of $k = 3.06$ along with a high variability as indicated by a scatter range $T_N = 5.29$ and the adjusted standard deviation for small samples $slogN_{corr} = 0.28$ (DIN 50100) and, thus, the steepest reduction in bearable stress amplitudes (Figure 5a). This results in a restricted time-to-failure range in which the stress amplitude must be reduced considerably to achieve a required number of load cycles. At a reference cycle count of 1.E+06 load cycles, only about 30 MPa of applied stress can be sustained at a median probability of failure ($P_A = 50\%$).

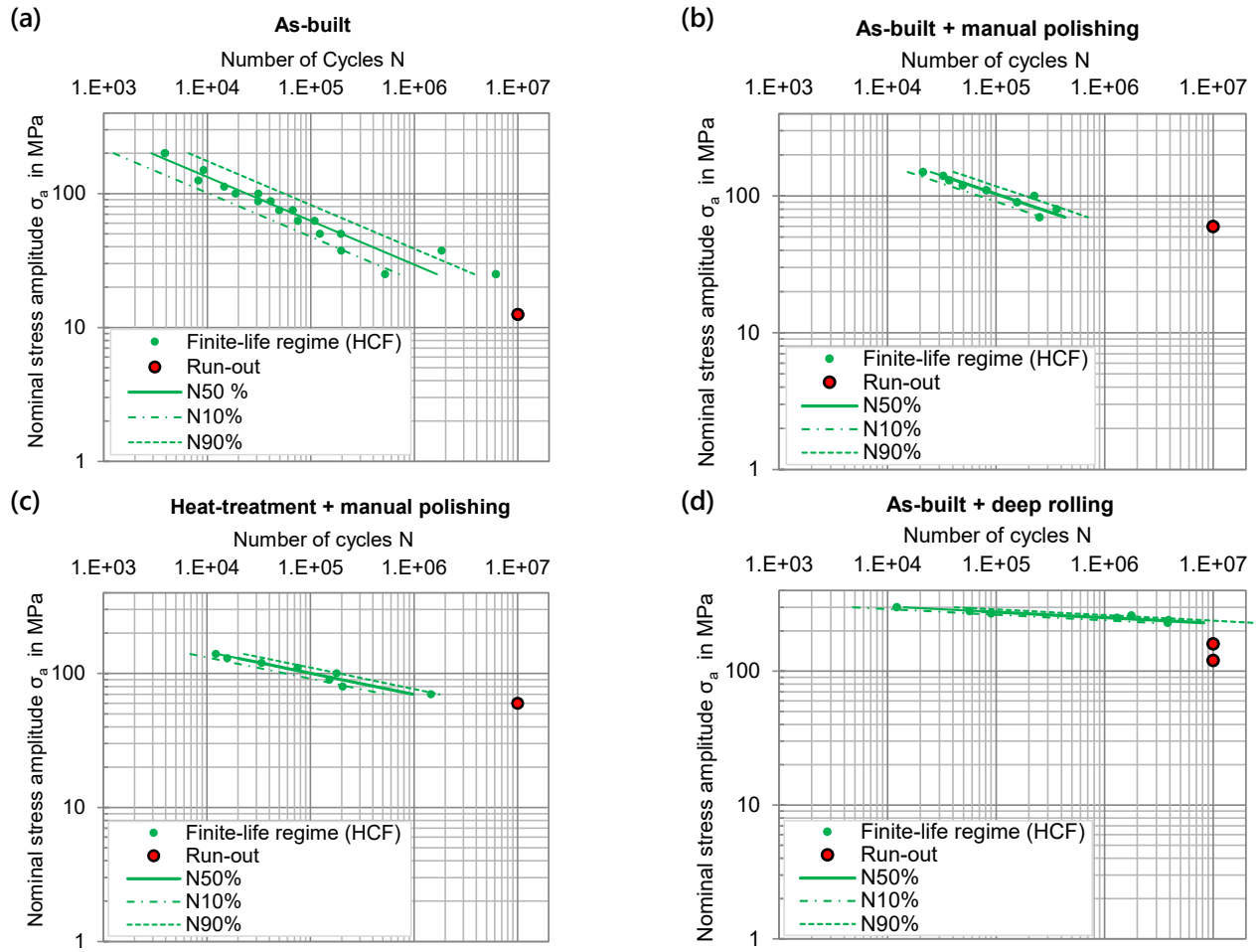

Figure 5 – Fatigue testing results shown as S–N curves including 10%, 50%, and 90% failure probabilities: *(a) illustrates the performance for the condition as-built. (b) illustrates the impact of manual polishing on the bearable stress amplitude. (c) shows that heat treatment and manual polishing lead to a further increase in stress amplitude in comparison to (a) and (b). (d) shows that combining as-built and deep rolling enables the highest bearable stress amplitudes across the finite-life range.*

ABMP specimens feature only a slightly improved slope of the S-N curve with $k = 3.73$ but much less variability with a scatter band of $T_N = 2.64$ ($slogN_{corr} = 0.16$) (Figure 5b). Due to the apparent parallel shift of the curve, a higher level of sustainable stress can be achieved. The determined run-out stress of 60 MPa, combined with the low scatter, indicates an increase in the fatigue strength due to mechanical polishing.

Compared to the ABMP condition, stress relief annealing in the HTMP condition flattens the S-N curve approximately by a factor of 2 featuring a slope of $k = 6.27$ (Figure 5c). This flattening is accompanied by an increase in variability with a scatter range $T_N = 3.30$ ($slogN_{corr} = 0.20$), since it is evaluated in the direction of cycle count rather than stress amplitude. The increased variability can be expected as we evaluate variability in the direction of cycle count rather than stress amplitude.

In the ABDR specimens, the inclination of the S–N curves is very flat (Figure 5d) with a slope of $k = 23.94$. We observe highest variability ($T_N = 8.60$, $slogN_{corr} = 0.36$) due to determining scatter in the finite life fatigue regime in the direction of the cycle number and not in the stress amplitude. However, the S-N curve spans the entire time-to-failure range within a nominal stress interval from 300 MPa to approximately 220 MPa. While this leads to a wide variation in the number of cycles to failure at a given nominal stress, it significantly expands the range of sustainable stress amplitudes. At 1.E+06 load cycles, a nominal stress of 251 MPa can be sustained (based on the median S-N curve, PA = 50%), representing an increase of approximately 7.8 times compared to the untreated AB condition. This pronounced flattening of the S-N curve also affects the lifetime range at lower cycle counts. At 2.E+04 load cycles, the sustainable stress amplitude increases from 106 MPa to 296 MPa, which is 2.8 times higher ($P_A = 50\%$). We observe similar results when combining heat treatment with deep rolling (HTDR), although with a less flat slope of the S-N curve is less flat featuring a slope of $k = 11.63$ (Figure A3). This change illustrates the reduction of basic strength caused by stress relief annealing.

Investigating fracture surfaces of ABMP samples, we observe that at lower amplitudes cracks originate at a single defect in the surface area (Figure 6a-d). Cracks grow in one plane until catastrophic fracture when the remaining load-bearing cross-section no longer withstands circumferential bending stress. At higher loads, cracks originate at various locations distributed around the circumference. However, starting again from small surface discontinuities, cracks begin to grow into the interior of the specimen across various planes. When catastrophic fracture occurs, specimens tear open across these various planes, resulting in a characteristic stepped fracture surface (Figure 6e-h). This behaviour is not visible for specimens where the surface was modified by deep rolling (Figure 6i-p).

3.5 Tensile testing and parameter identification

Specimens showed strain hardening and no distinct yield point (Figure 7). Additionally, it becomes evident that the heat-treated specimens exhibit larger elongation at fracture at significantly lower stress levels. Furthermore, the heat treatment appears to reduce the yield stress.

We identified the material parameters for the different specimen conditions using the nonlinear least-squares method. The fit between experiment and model response is illustrated in Figure 7e-f. The model response with the identified parameters agrees very well with the experimental data. The identified parameters are reported in Table 3. For all the identifications, we verified local uniqueness of the solution, as the smallest sub-determinant of the approximated Hessian was non-vanishing.

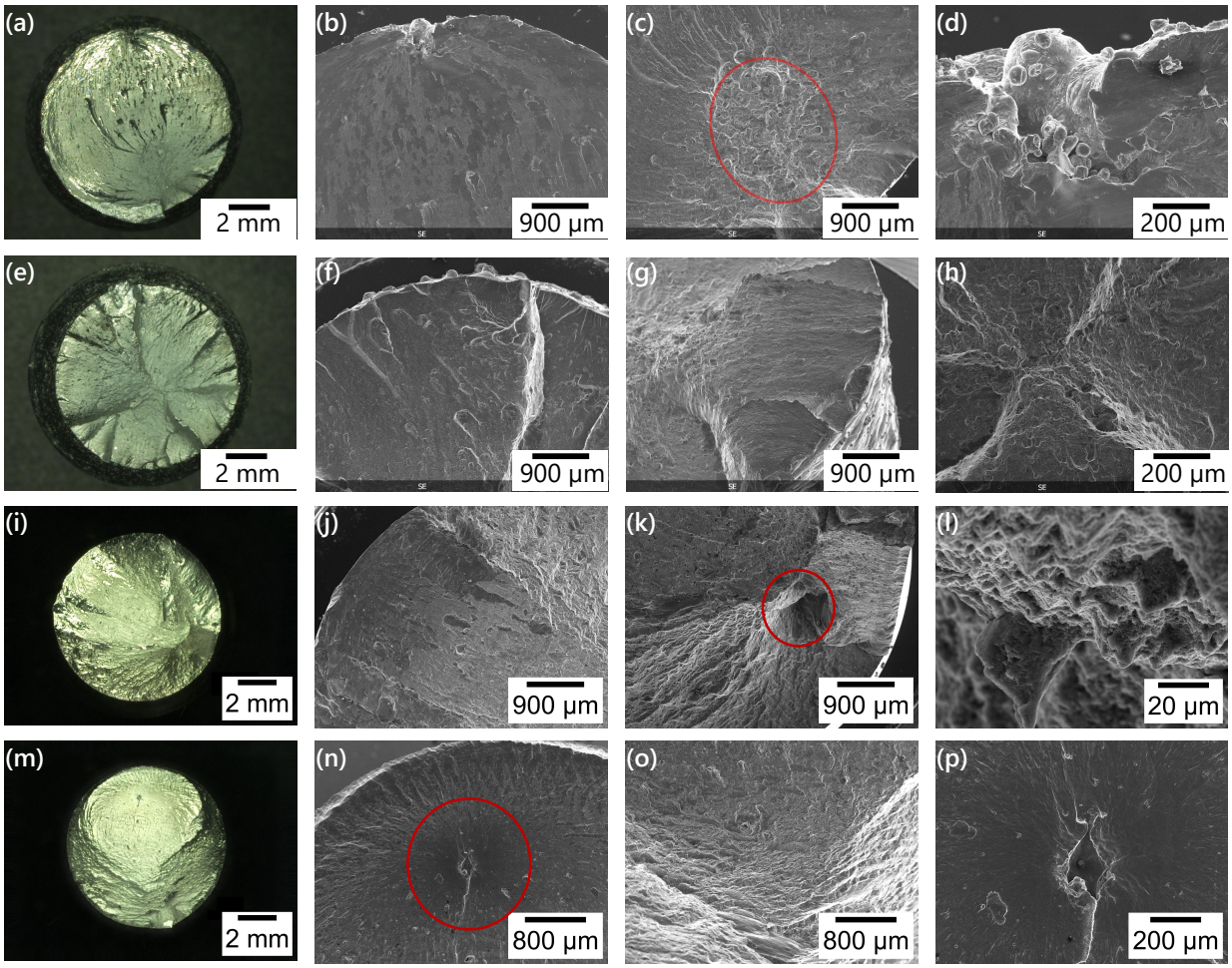

Figure 6 – Fracture surfaces of four exemplary rotational bending specimens: *(a-d) exemplary specimen of condition as-built + manual polishing tested at $\sigma_0 = 75$ MPa shows a fracture surface under low stress amplitudes. The crack initiation occurs at a single imperfection in the surface region. The crack growth takes place in a plane until a catastrophic failure (final fracture) occurs when the remaining load-bearing cross-section can no longer withstand the surrounding bending stresses. The red ellipse illustrates the residual fracture surface. (e-h) exemplary specimen of condition as-built + manual polishing tested at $\sigma_0 = 137.5$ MPa, exemplifying the fracture behaviour under high stress amplitudes. Crack initiation occurs at various locations distributed around the circumference. Originating from smaller superficial imperfections, cracks begin to grow inward through different planes within the sample. Upon the occurrence of final fracture, the sample tears along these various planes, resulting in a characteristic stair-step fracture surface. (i-p) two exemplary specimens if condition as built + deep rolling show that deep rolling alters the fracture surface and the aforementioned behaviour cannot be observed. Red ellipses illustrate again the "residual fracture surface".*

The identified parameters clearly quantify the lower yield stress for the HTMP-specimens, which is observed during tensile testing. Additionally, the ABDR-specimens exhibit higher stiffness and larger nonlinear hardening parameters. While the latter are difficult to interpret, they indicate a more pronounced hardening behaviour during tensile testing.

Because of the specimen geometry, a homogeneous uniaxial tensile stress state is not achievable during tensile testing. The curved testing region inevitably introduces shear stresses. The shear stress impact is investigated by numerical finite element analysis. We discretised the nominal specimen geometry with 20-noded hexahedral elements. The boundary conditions and spatial discretisation are illustrated in Figure 8a. The prescribed axial displacement leads to an axial strain of approximately 3.5 % when using the same strain computation procedure as in the experiment. This is done to pre-

vent extrapolation since the material parameters for the as-built material were determined at a maximum axial strain of 3.5 %. The axial stress is computed as in the experiment using the axial reaction force in the nonlinear finite element analysis. Consequently, because of the three-dimensional stress state, the axial stress-axial strain curve for the specimen differs from the one in the parameter identification above, although the same parameters were used.

Table 3 – Identified elasto-plastic material parameters using quasi-static tensile tests

Condition	E in MPa	$\hat{k}$ in MPa	b	c in MPa
AB	63085 ± 488	226.43 ± 1.56	61.08 ± 2.01	10470 ± 246
ABMP	65686 ± 357	223.17 ± 1.44	102.70 ± 4.44	14111 ± 405
HTMP	61337 ± 2310	125.22 ± 3.98	131.13 ± 5.59	11799 ± 753
ABDR	72080 ± 332	211.75 ± 1.37	181.36 ± 4.98	23655 ± 544

We evaluated stress coefficients $s_{zx,i} = \sigma_{zx}/\sigma_{zz}$ and $s_{xy,i} = \sigma_{xy}/\sigma_{zz}$ for all integration points i adjacent to the smallest cross section of the specimen. Figure 8d shows the maximum stress ratios $\max|s_{zx,i}|$ and $\max|s_{xy,i}|$.

The shear impact due to non-optimal specimen shape was noticeable (Figure 8). After 3% axial strain, the stress coefficients $s_{zx,i} = \sigma_{zx}/\sigma_{zz}$ and $s_{xy,i} = \sigma_{xy}/\sigma_{zz}$ deviate by 2% and 6%, respectively. Thus, no perfectly uniaxial tensile stress state is present during quasi-static tensile testing. However, because of the comparably small ratio between axial tensile stress and shear stress, we assume that this influence can be neglected during the material parameter identification and the procedure described in Section 2.7.2 remains valid. Moreover, since we perform the same procedure for all specimen conditions, the results are comparable between the different groups.

During the quasi-static tensile testing, partial unloading was performed multiple times as illustrated in Figure 2. The unloading enables quantification of a structural modulus M from the slope of the force-displacement curve during unloading and subsequent reloading (Figure 9a). Damage is defined as $D = 1 - M_i/M_0$, $i = 0, \dots, n$, where n denotes the number of partial unloading. Significant reductions in the structural modulus were detectable at the beginning of the plastic deformation (Figure 9). All specimens showed a rapid increase in continuum damage after passing the yield point. Thereafter, damage accumulation slowed down but never stopped entirely until failure.

4 Discussion

We explored pathways to enhance the lifespan of additively manufactured AlSi10Mg through surface treatment. Our post-treatment process aims to enhance the surface without employing subtractive processes involving geometrically defined cutting tools, such as turning or milling. This approach optimally utilises the potential of additive manufacturing to directly generate the final contour and the capability of surface enhancements to improve material lifespan.

We measured and compared the residual stresses in the different conditions (Figure A2). The anisotropic residual stress distribution observed in the AB state is characteristic of PBFLB and arises from the layer-wise scan strategy and steep thermal gradients [34]. The substantial tensile residual stresses of about 200 MPa in the z-direction of the ABMP condition extend over a depth of approximately 0.4 mm from the surface, which corresponds to the thickness of the α-Al-rich surface layer. Even when

stress-relief annealing reduces the bulk tensile stresses, the as-built surface does not form a homogeneous plane; local inhomogeneities such as roughness, partially melted particles and surface oxidation can generate a narrow tensile peak around 0.1 mm (Figure A2) [8,35]. Roller burnishing (ABDR) converts the initial tensile residual stresses into beneficial compressive stresses but introduces an unexpected anisotropy: the compressive stress is stronger in the build direction (z, -350 MPa), than in the scan direction (y, -240 MPa). This behaviour cannot be explained by a simple superposition of initial and induced stresses. Instead, it reflects the anisotropic microstructure and the direction-dependent mechanical properties of PBF-LB materials, which cause different accommodation of the imposed plastic deformation in z and y and thereby overcompensate the higher initial tensile stress in the build direction [36,37].

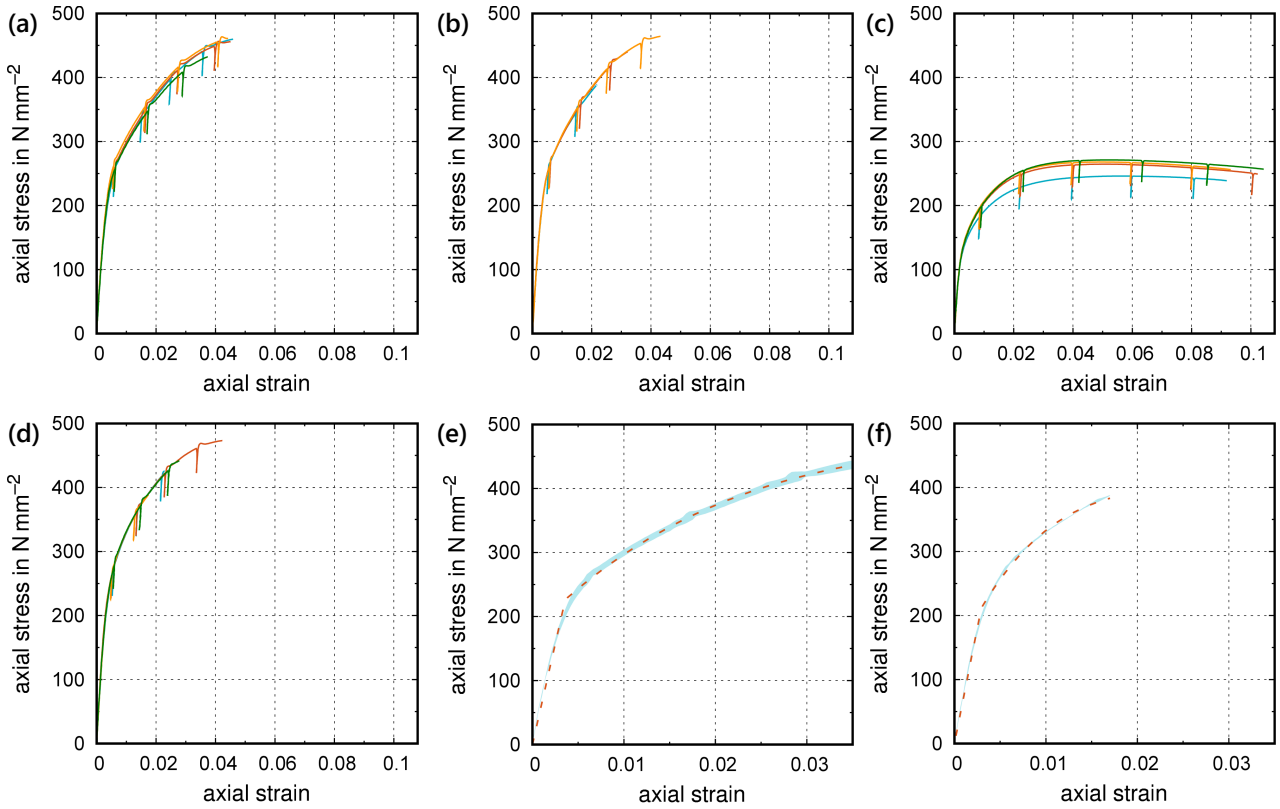

Figure 7 – Tensile test results. *Stress and strain curves feature an initial linear-elastic region, a smooth transition into the plastic region (i.e. no distinct yield point), followed by monotonic hardening. Clearly visible are the partial unloading curves that allowed us to evaluate continuum damage evolution. Conditions shown are (a) AB, (b) ABMP, (c) HTMP, and (d) ABDR. (e) illustrates the fit of the parameter identification on the experimental data as mean (red) with standard deviation (turquoise) for AB and (f) for condition ABDR.*

Overall, the S-N curve in the AB condition begins with high inherent strength and shows a sharp drop in fatigue life as the stress amplitude decreases (Figure 6a), as highlighted by the steep slope ($k = 3.06$) of the S-N curve (Figure 5). The AB condition exhibits relatively high strength post-manufacturing (Figures 4 and 6). However, the permissible number of load cycles at low stress amplitudes was observed to be low, which may have been caused by the low ductility of the material (Figure 5). Once damage initiates, rapid failure typically occurs.

We can also attribute the increased scatter of the AB samples to the chosen specimen geometry. If the gauge length – where the waist of the specimen concentrates stresses – contains less pronounced surface irregularities, the specimens tend to last longer. In contrast, a cylindrical test cross-section subjected to a trapezoidal bending moment (four-point bending) would increase the probability of critical irregularities occurring, which ultimately positively influences the scatter. Conversely, this

means that the chosen specimen geometry tends to yield slightly higher lives, a factor we should consider when interpreting the results. Nevertheless, surface defects and manufacturing-related irregularities may be starting points for mesoscopic cracks as shown in Figure 6.

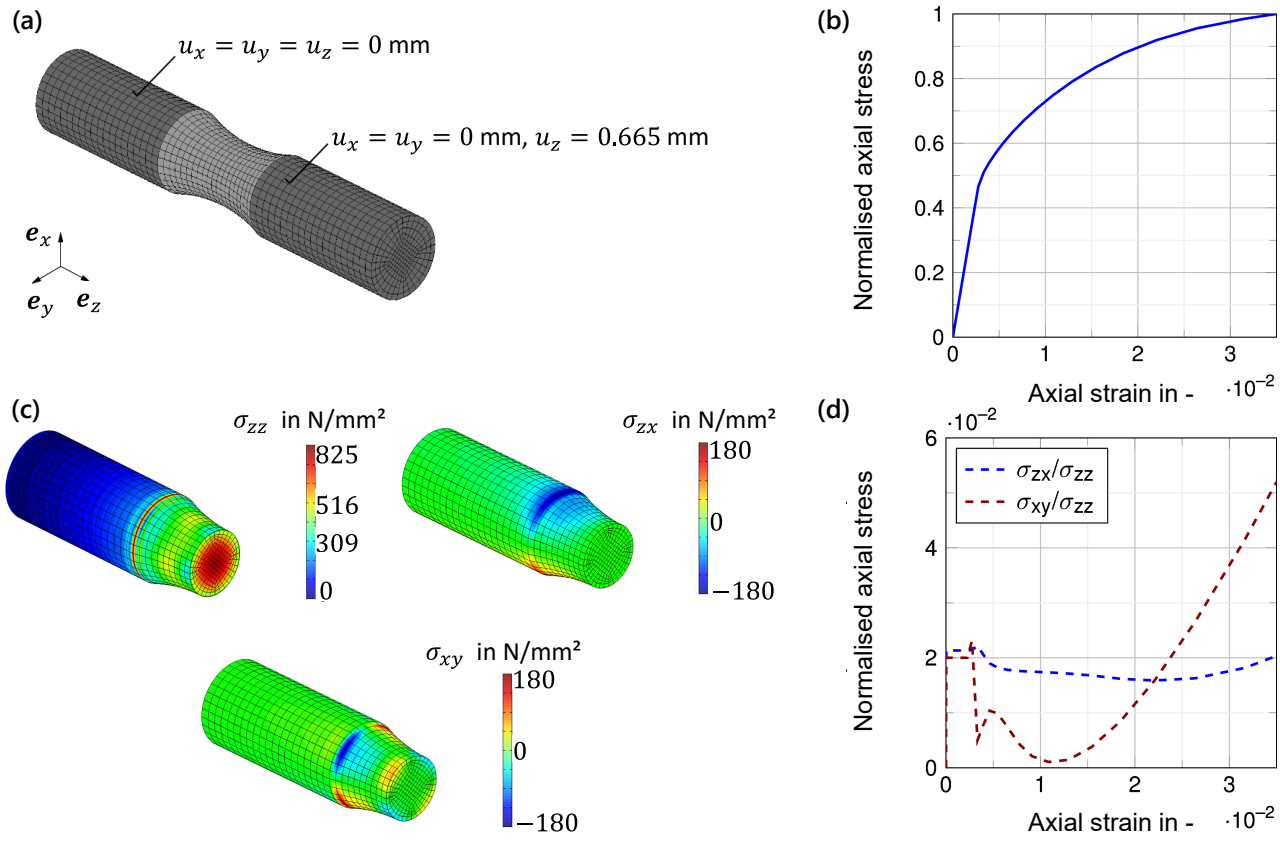

Figure 8: *(a) shows the FE mesh for the fatigue testing geometry with boundary conditions for quasi-static tensile testing. (b) shows an exemplary stress-strain curve normalised to maximum stress. (c) illustrates stress components σ_{zz}, σ_{zx}, and σ_{xy}. Here, σ_{zy} is not visualised as it is equal to by but rotated with 90° with respect to the specimen's axis. (d) stress coefficients $s_{zx,i} = \sigma_{zx}/\sigma_{zz}$ and $s_{xy,i} = \sigma_{xy}/\sigma_{zz}$ are evaluated for all integration points i adjacent to the smallest cross section. The figure shows the maximum stress ratios $max\ |s_{zx,i}|$ and $max\ |s_{xy,i}|$ and, thus, illustrates the amount of shear triggered by uniaxial loading.*

Manual polishing effectively removes coarse irregularities from the surface (Figure 3). Mechanical surface levelling causes a parallel shift of the S-N curve higher fatigue lives. Smoothing the surface minimises the micro-notch effect caused by the rough and less ductile surface, so crack initiation only commences at higher stress amplitudes. However, the damage mechanisms in the base material remain unchanged. The slope of the S-N curve ($k = 3.73$) is only slightly different from the AB state. However, the considerably reduced variability points to a much more stable behaviour under load.

Solution annealing at 325 °C for 2 hours, followed by air cooling (HTMP), helps to improve the performance, as indicated by the flatter inclination of the S-N curve ($k = 6.27$). Annealing helps to reduce residual stresses and is known to enhance material lifespan under low stress amplitudes [19,38–40]. The fast cooling rates during the LPBF process strongly influence the mechanical properties of AlSi10Mg [1, 2]. In the untreated AB state, the material exhibits high strength, which is due to a fine microstructure (Figure 4, Figure A4). This microstructure consists of cellular α-Al structures that are surrounded by a network of eutectic Si. The fine Si particles and cell boundaries act as strengthening mechanisms, resulting in significantly higher yield strength, tensile strength, and microhardness compared to conventionally cast AlSi10Mg. Simultaneously, this microstructure limits ductility because

the brittle Si network provides locations for crack formation and promotes ductile-brittle failure behaviour [19,40,41]. To improve ductility, heat treatment is frequently utilised. During this process, the eutectic silicon cell walls collapse, and a needle-shaped Mg_2Si precipitation phase forms within the α-Al (Figure 4, Figure A5). Although this microstructural change reduces strength, it significantly increases the material's ductility [19] as can be seen in Figure 7. In an effort to exploit this, we used a heat treatment protocol for stress-relief annealing. However, the impact on the lifespan performance observed here is limited as the improvement of the slope of the S-N curve is only a factor of ~2. This suggests that the detrimental effect of surface irregularities, which cannot be fully removed by polishing (Section 3.1), is more dominant than manufacturing-induced residual stresses.

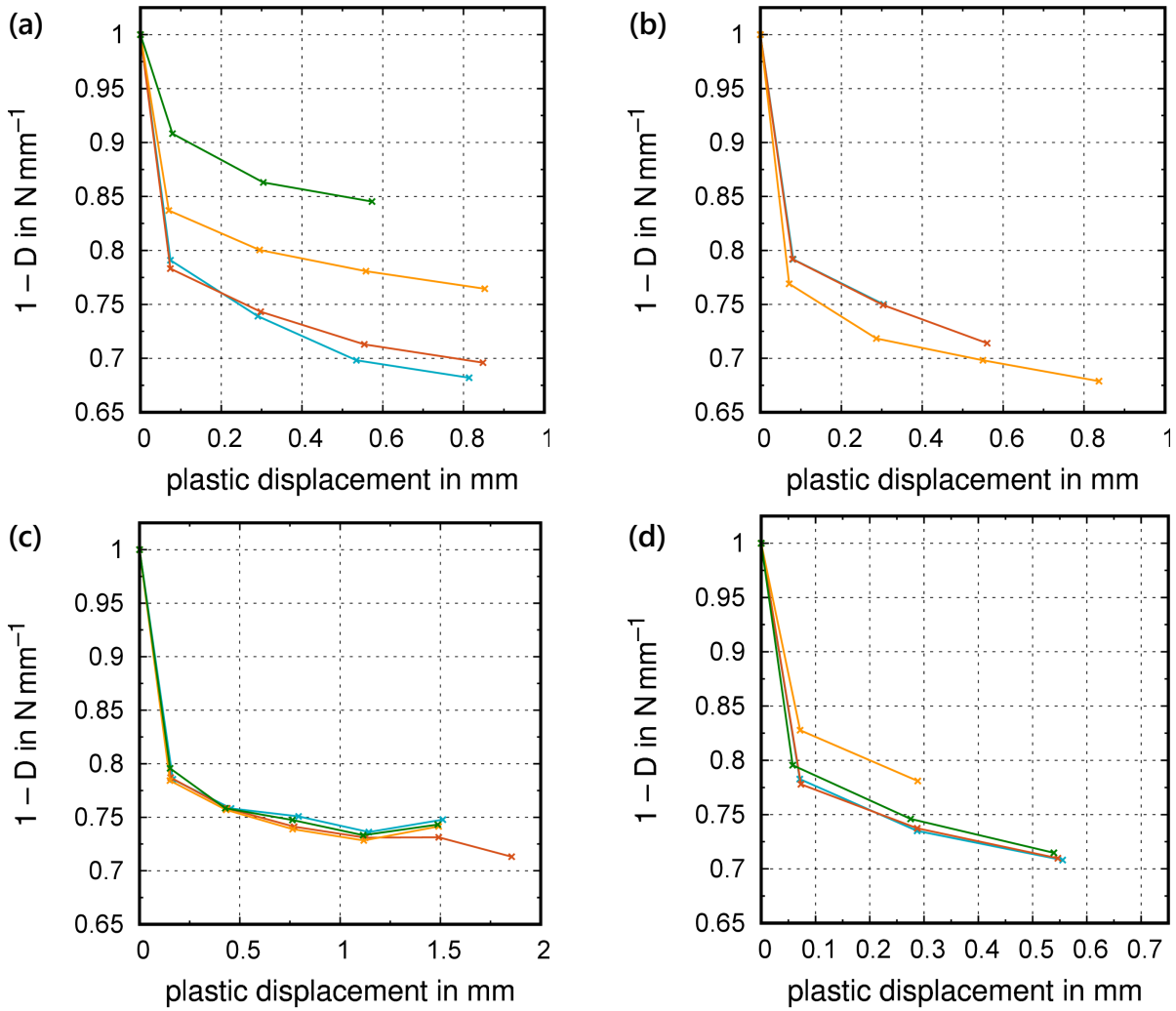

Figure 9 – Damage evolution during quasi-static overloading: *(a) damage evolution for the as-built (AB) condition. (b) damage evolution for condition as-built + manual polishing (ABMP). (c) damage evolution for heat-treated as-built specimens (HTMP). (d) damage evolution for as-built + deep rolling (ABDR).*

Changing the modification of the surface topography helps to reduce the detrimental notch effect of defects and manufacturing-related irregularities. Deep rolling removes notches and irregularities at the surface that could not be removed by mechanical polishing. Deep rolling significantly alters the mechanical properties of the treated material. Its influence on the surface hardening profile is illustrated in Figure 3, showing an affected depth of 0.8 mm. Furthermore, this process induces compressive residual stresses that counteract crack initiation and propagation (Figure 6), positively influencing lifespan [42,43]. Consequently, damage only initiates at significantly higher stress amplitudes, which allows the material to permanently endure stresses exceeding 200 MPa (Figure 5) across the

entire finite life fatigue regime. This means the material can permanently endure stresses in the range of the yield strength of the AB state. The pronounced flattening of the S-N curve at lower cycle counts, however, is beneficial as components treated by deep rolling could be used at comparatively high nominal stress amplitudes, especially when long lifetimes are required. It appears plausible that the local plastic deformation of the material due to the process reduces the damaging effect of the eutectic silicon network at the grain boundaries by destroying or reforming it. We can achieve a similar effect through thermomechanical deformation, such as in the friction stir process [44].

While we concentrated on deep rolling, other methods such as shot peening allow for flexibility with specimen surfaces and used media, which, in turn, allow it to achieve similar results on surfaces that are not rotational symmetric. Applying deep rolling to the as-built condition changed the surface topography without sacrificing tensile strength (Figure 7). Removing surface irregularities and inducing residual stresses in the surface has a positive effect on lifespan performance as evidenced by the much flatter slope of the S-N curve ($k = 23.94$) and the much higher bearable stress amplitudes (Table 2).

We measured surface roughness to enable a quantitative comparison of surface condition (Figure 3). We determined the mean roughness R_Z. The as-built specimens showed the highest roughness, attributable to the layer-by-layer nature of additive manufacturing. This high roughness is expected to amplify the notch effect in the already notched specimens, leading to reduced fatigue life. Manual grinding of the surface markedly lowered roughness and therefore improved fatigue performance. However, two measurements of the manually ground condition indicate that reproducing an identical finish by hand is difficult. Deep rolling delivered the best surface condition, with $R_Z = 0.57$ µm, producing an almost smooth surface while being reproducible. Consequently, the notch effect is largely mitigated, enabling good fatigue performance at high stress levels in specimens conditioned ABDR and HTDR.

Heat treatment counteracted this development in comparison to the ABDR condition as shown by a steeper slope of the S-N curve ($k = 11.63$) and lower levels of bearable stress amplitudes. Solution annealing may have resolved residual stresses that are beneficial for lifespan enhancement and while the S-N curve of the condition heat treatment + deep rolling may be lower (~factor 2), it is still superior to those of the as-built and heat treatment conditions. Results clearly indicate the positive effect of removing surface irregularities, enhancing the surface topography, and its properties.

This is supported by our hardness testing, which shows that deep rolling has a beneficial effect on the surface properties (Figure 3). Overall, the deep rolling condition delivers the best results and represents an economical method of achieving desirable service life properties. This condition only requires mechanical surface treatment, which can also be performed manually. Due to the resulting excellent properties, heat treatment becomes unnecessary, as it does not provide any additional beneficial effects. Eliminating heat treatment also saves time and energy costs. In addition to all the positive effects, deep rolling offers the advantage of being reproducible and automatable. This is particularly true for rotationally symmetrical components, so that a mechanical surface treatment such as deep rolling appears to be a good choice.

Overall, the run-out specimens included in the S-N curves form part of the string-of-pearl procedure, but we excluded them from the evaluation according to DIN 50100. Since we did not explicitly analyse the transition to the endurance limit in this investigation, we can only utilise these run-out specimens as a rough guide. Due to the limited sample size, we adjusted the standard deviation using a

correction factor for small samples ($slogN_{corr}$) in order to determine the scatter band (T_N) more accurately. The fatigue tests show clear trends regarding the individual material states. However, because of the limited data basis, we should also interpret the determined characteristic parameters (slope k and scatter band T_N) with care.

Tensile properties as measured here should be taken with a pinch of salt. The specimens we used resemble the same dumbbell shape as those subjected to fatigue testing. This has two reasons: (i) we wanted to compare the tested conditions as is and (ii) we had to address a shortage in samples and materials. Since these tests are not using ISO norm specimens, we resorted to a computational parameter identification (Section 2.7) building on established protocols for parameter estimation [28]. The good agreement between model response and experiments (Section 3.3) indicate that the estimates are usable. To assess the shear impact resulting from the dumbbell-shaped specimen, we have analysed a tensile test computationally (Figure 8). Maximum stress coefficients $s_{zx,max} = \sigma_{zx}/\sigma_{zz}$ and $s_{xy,max} = \sigma_{xy}/\sigma_{zz}$ range between 0.02 and 0.06 between 0% and 3% tensile strain (ε_{zz}). While not negligible, we consider this impact as small enough to allow comparison of the conditions. Overall, tensile strength (or maximum stresses) as determined here agrees with known strengths for this material (450 - 598 MPa) [45–48]. Stiffness as identified by our inverse computational approach fits to the literature (~61 - 72 GPa) [49,50]. The overall stress-strain response of the specimens is comparable to the data reported by [51,52]. Therefore, we conclude that while not ideal, our procedure of computing stress and strain and the results of these quasi-static tests are usable for the comparisons made in this study. Compared to [51], the agreement between experiments and numerical model response is even improved in this work. Heat treatment significantly reduces ultimate strength and changes the characteristics of the post-yield behaviour, which agrees well with the findings reported by [51,52]. Gebhardt et al. [51] attributed this behaviour to microstructural coarsening that dominates the formation of precipitates. Similar behaviour has been observed previously for additively manufactured AlSi10Mg [52,53].

We attribute damage accumulation (Figure 9) to the manufacturing process. Additive manufacturing is known to deliver production-induced heterogeneous microstructures as well as pores [48,53]. This effect is similar to the surface heterogeneities, but unlike them, cannot be removed by improving the surface topography. All curves show a noticeable settling between 0 mm and 0.1 mm plastic displacement. Thereafter, damage accumulation slows down. Our results indicate that adapting the surface removes the variability when comparing AB specimens with those from other conditions. Changing the surface topography may not be detectable in quasi-static tensile strength and stiffness (Figure 7) as the affected cross-sectional area is only a thin peripheral annulus (Figure 3) and, thus, small in comparison to the sample diameter. The removal of detrimental irregularities and the enhancement of mechanical properties where bending stresses are highest (Figure 3) changes the characteristic how cracks move across the specimen cross section (Figure 6). Therefore, these widely available techniques seem to be beneficial.

5 Conclusion

Additively manufactured AlSi10Mg components impress with their versatility and widespread use across various industries. However, the fatigue properties of such components remain a critical weakness. To address this, we investigated ways to improve fatigue life through deep rolling. Our results demonstrate that fatigue performance can be significantly enhanced using simple post-processing techniques that modify the surface without relying on subtractive methods involving geometrically defined cutting tools, such as turning or milling. At the same time, the surface generated during the

manufacturing process is positively influenced. Heat treatment is not required and may even have adverse effects.

With the proposed approach of mechanical post-processing via deep rolling, prototype components for pre-series models can be safely deployed without the risk of failures of additively manufactured parts during early testing phases. This method optimally combines the potential of additive manufacturing—such as the ability to produce near-net-shape components—with directly applicable surface enhancement techniques to reliably improve material lifespan.

Acknowledgement

The study was supported by Volkswagen AG where Andreas Krevet is currently employed.

Declaration of generative AI and AI-assisted technologies in the manuscript preparation process

During the preparation of this work, we used scienceos.ai in order to research resources, conduct deep dives into specific topics to aid discussion, translate texts from German to English as well as to check coherence, cohesion, and grammar of the written content. After using this tool, we critically reviewed and edited the manuscript as needed and we take full responsibility for the content of the published article. AI and AI-assisted technologies were not used as an "author".

6 Bibliography

[1] V. Bhavar, P. Kattire, V. Patil, S. Khot, K. Gujar, R. Singh, A review on powder bed fusion technology of metal additive manufacturing, in: A.B. Badiru, V.V. Valencia, D. Liu (Eds.), Addit. Manuf. Handb., 1st ed., CRC Press, 2017: pp. 251–253. https://doi.org/10.1201/9781315119106-15.

[2] L. Ladani, M. Sadeghilaridjani, Review of Powder Bed Fusion Additive Manufacturing for Metals, Metals 11 (2021) 1391. https://doi.org/10.3390/met11091391.

[3] N. Read, W. Wang, K. Essa, M.M. Attallah, Selective laser melting of AlSi10Mg alloy: Process optimisation and mechanical properties development, Mater. Des. 1980-2015 65 (2015) 417–424. https://doi.org/10.1016/j.matdes.2014.09.044.

[4] D. Manfredi, From Powders to Dense Metal Parts: Characterization of a Commercial AlSiMg Alloy Processed through Direct Metal Laser Sintering, Materials 6 (2013) 856–869. https://doi.org/10.3390/ma6030856.

[5] R. Revilla, Local Corrosion Behavior of Additive Manufactured AlSiMg Alloy Assessed by SEM and SKPFM, J. Electrochem. Soc. 164 (2017). https://doi.org/10.1149/2.0461702JES.

[6] B. Martin, Aging and strength of bone as a structural material, Calcif. Tissue Int. 53 (1993) S34–S40.

[7] E. Maleki, Application of gradient severe shot peening as a novel mechanical surface treatment on fatigue behavior of additively manufactured AlSi10Mg, Mater. Sci. Eng. (2023). https://doi.org/10.1016/j.msea.2023.145397.

[8] A.H. Maamoun, M.A. Elbestawi, S.C. Veldhuis, Influence of Shot Peening on AlSi10Mg Parts Fabricated by Additive Manufacturing, J. Manuf. Mater. Process. 2 (2018) 40. https://doi.org/10.3390/jmmp2030040.

[9] T. Rautio, A. Hamada, J. Kumpula, A. Järvenpää, The effect of shot peening on corrosion performance of anodized laser powder bed fusion manufactured AlSi10Mg, IOP Conf. Ser. Mater. Sci. Eng. 1234 (2022) 012035. https://doi.org/10.1088/1757-899X/1234/1/012035.

[10] T. Rautio, M. Hietala, A. Järvenpää, Enhancing Surface Properties of AM AlSi10Mg Components: A Study on Shot Peening and Silver Shell-Copper Core Coating, Key Eng. Mater. 992 (2024) 93–99. https://doi.org/10.4028/p-bUUn7X.

[11] N. Stelzer, T. Sebald, M. Hatzenbichler, B. Bonvoisin, B. Lubos, M. Scheerer, Properties of Surface Engineered Metallic Parts Prepared by Additive Manufacturing, (2021). https://doi.org/10.20944/preprints202102.0128.v1.

[12] A.D. Brandão, J. Gumpinger, M. Gschweitl, C. Seyfert, P. Hofbauer, T. Ghidini, Fatigue Properties Of Additively Manufactured AlSi10Mg – Surface Treatment Effect, Procedia Struct. Integr. 7 (2017) 58–66. https://doi.org/10.1016/j.prostr.2017.11.061.

[13] N. Sato, M. Matsumoto, H. Ogiso, H. Sato, Advanced Manufacturing Research Institute (AMRI), National Institute of Advanced Industrial Science and Technology (AIST) 1-2-1 Namiki, Tsukuba, Ibaraki 305-8564, Japan, Challenges of Remanufacturing Using Powder Bed Fusion Based Additive Manufacturing, Int. J. Autom. Technol. 16 (2022) 773–782. https://doi.org/10.20965/ijat.2022.p0773.

[14] N. Zhang, S.R. Kandavalli, C. Gode, H. Kong, S. Attarilar, M. Ebrahimi, S.R. Kandavalli, M. Shamsborhan, H. Jafarzadeh, S. Jannet, Thermal treatments of titanium- and nickel-based alloys processed by powder bed fusion technology, Can. Metall. Q. 64 (2025) 758–785. https://doi.org/10.1080/00084433.2024.2359317.

[15] E. Brandl, Additive manufactured AlSi10Mg samples using Selective Laser Melting (SLM): Microstructure, high cycle fatigue, and fracture behavior, Mater. Des. 34 (2012) 159–169. https://doi.org/10.1016/J.MATDES.2011.07.067.

[16] A. Mertens, Fusion-Based Additive Manufacturing for Processing Aluminum Alloys: State-of-the-Art and Challenges, Adv. Eng. Mater. 19 (2017). https://doi.org/10.1002/adem.201700003.

[17] S.C. Altıparmak, Challenges in additive manufacturing of high-strength aluminium alloys and current developments in hybrid additive manufacturing, Int. J. Lightweight Mater. Manuf. 4 (2021) 246–261. https://doi.org/10.1016/j.ijlmm.2020.12.004.

[18] T. DebRoy, Additive manufacturing of metallic components – Process, structure and properties, Prog. Mater. Sci. 92 (2018) 112–224. https://doi.org/10.1016/J.PMATSCI.2017.10.001.

[19] A. Kumar Ramavajjala, T.R. Dandekar, R.K. Khatirkar, C. Joshi, R.N. Chouhan, A. Agnihotri, A review on the correlation between microstructure, heat treatment and mechanical properties of additively manufactured AlSi10Mg by LPBF, Crit. Rev. Solid State Mater. Sci. 50 (2025) 239–274. https://doi.org/10.1080/10408436.2024.2414012.

[20] F.A. Milaat, P. Witherell, M. Hardwick, H. Yeung, V. Ferrero, L. Monnier, M. Brown, STEP-NC Process Planning for Powder Bed Fusion Additive Manufacturing, J. Comput. Inf. Sci. Eng. 22 (2022) 060904. https://doi.org/10.1115/1.4055855.

[21] P. Wang, G. Robertson, B.T. Gibson, C.M. Fancher, J. Reynolds, M. Borish, J.R. Cruz, P. Chesser, B. Stump, A. Jackson, E. MacDonald, Improved Productivity with Multilaser Rotary Powder Bed Fusion Additive Manufacturing, 3D Print. Addit. Manuf. 11 (2024) 231–241. https://doi.org/10.1089/3dp.2022.0288.

[22] M.K. Niaki, Economic sustainability of additive manufacturing, J. Manuf. Technol. Manag. (2019). https://doi.org/10.1108/JMTM-05-2018-0131.

[23] R. Huang, Environmental and Economic Implications of Distributed Additive Manufacturing: The Case of Injection Mold Tooling, J. Ind. Ecol. 21 (2017). https://doi.org/10.1111/jiec.12641.

[24] N. Gadlegaonkar, P.J. Bansod, A. Lakshmikanthan, K. Bhole, A Review on Additively Manufactured AlSi10Mg Alloy: Mechanical, Tribological, and Microstructure Properties, J. Mines Met. Fuels (2025) 87–101. https://doi.org/10.18311/jmmf/2025/46621.

[25] G. Petzow, Metallographisches, Keramographisches, Plastographisches Ätzen, 7 leicht korrigierte Aufl, Borntraeger, Stuttgart, 2015.

[26] U. Jung, R. Schaal, C. Berger, H. -W. Reinig, H. Traiser, Berechnung der Schwingfestigkeit festgewalzter Kurbelwellen, Mater. Werkst. 29 (1998) 569–572. https://doi.org/10.1002/mawe.19980291006.

[27] C. Rohrbach, Handbuch für experimentelle Spannungsanalyse, Springer-Verlag, 2013.

[28] U. Römer, S. Hartmann, J.-A. Tröger, D. Anton, H. Wessels, M. Flaschel, L. De Lorenzis, Reduced and All-At-Once Approaches for Model Calibration and Discovery in Computational Solid Mechanics, Appl. Mech. Rev. 77 (2025) 040801. https://doi.org/10.1115/1.4066118.

[29] S. Hartmann, P. Haupt, Stress computation and consistent tangent operator using non-linear kinematic hardening models, Int. J. Numer. Methods Eng. 36 (1993) 3801–3814. https://doi.org/10.1002/nme.1620362204.

[30] M. Costas, D. Morin, M. De Lucio, M. Langseth, Testing and simulation of additively manufactured AlSi10Mg components under quasi-static loading, Eur. J. Mech. - ASolids 81 (2020) 103966. https://doi.org/10.1016/j.euromechsol.2020.103966.

[31] J. Tröger, U. Römer, S. Hartmann, Comparing frequentist and Bayesian uncertainty quantification in two-step constitutive model calibration, PAMM 24 (2024) e202400031. https://doi.org/10.1002/pamm.202400031.

[32] M. Beder, S.B. Akçay, T. Varol, H. Çuvalcı, The Effect of Heat Treatment on the Mechanical Properties and Oxidation Resistance of AlSi10Mg Alloy, Arab. J. Sci. Eng. 49 (2024) 15335–15346. https://doi.org/10.1007/s13369-024-08971-1.

[33] J. Shan, X. Xin, C. Zhang, G. Cao, L. Yang, G. Huang, Microstructural Analyses of Inter-Granular Corrosion Behavior for 6082-T6 Aluminum Alloy, IOP Conf. Ser. Mater. Sci. Eng. 301 (2018) 012074. https://doi.org/10.1088/1757-899X/301/1/012074.

[34] A. Salmi, E. Atzeni, History of residual stresses during the production phases of AlSi10Mg parts processed by powder bed additive manufacturing technology, Virtual Phys. Prototyp. 12 (2017) 153–160. https://doi.org/10.1080/17452759.2017.1310439.

[35] L. Strauß, G.A. Pang, G. Löwisch, Fatigue life prediction of additively manufactured AlSi10Mg based on surface roughness and residual stress, Fatigue Fract. Eng. Mater. Struct. 47 (2024) 4465–4477. https://doi.org/10.1111/ffe.14441.

[36] M.E. Daoud, I. Taha, A. Abdelgawad, I. Barsoum, K.A. Khan, D.H. Anjum, Mapping residual stresses in AlSi10Mg alloy fabricated by powder bed fusion-laser beam method, Sci. Rep. 15 (2025) 24784. https://doi.org/10.1038/s41598-025-09316-0.

[37] F. Sajadi, J.-M. Tiemann, N. Bandari, A. Cheloee Darabi, J. Mola, S. Schmauder, Fatigue Improvement of AlSi10Mg Fabricated by Laser-Based Powder Bed Fusion through Heat Treatment, Metals 11 (2021) 683. https://doi.org/10.3390/met11050683.

[38] N.T. Aboulkhair, I. Maskery, C. Tuck, I. Ashcroft, N.M. Everitt, The microstructure and mechanical properties of selectively laser melted AlSi10Mg: The effect of a conventional T6-like heat treatment, Mater. Sci. Eng. A 667 (2016) 139–146. https://doi.org/10.1016/j.msea.2016.04.092.

[39] A. Gatto, C. Cappelletti, S. Defanti, F. Fabbri, The Corrosion Behaviour of Additively Manufactured AlSi10Mg Parts Compared to Traditional Al Alloys, Metals 13 (2023) 913. https://doi.org/10.3390/met13050913.

[40] S. Megahed, J. Bühring, T. Duffe, A. Bach, K.-U. Schröder, J.H. Schleifenbaum, Effect of Heat Treatment on Ductility and Precipitation Size of Additively Manufactured AlSi10Mg, Metals 12 (2022) 1311. https://doi.org/10.3390/met12081311.

[41] B. Atar, E. Üyüklü, P. Yayla, Microstructure and mechanical properties of an additively manufactured AlSi10Mg based alloy, Mater. Test. 65 (2023) 874–885. https://doi.org/10.1515/mt-2022-0334.

[42] I. Kim, S.C. Park, Y.I. Kim, D.-K. Kim, K.-A. Lee, S.J. Oh, B. Lee, Surface residual stress analysis of additive manufactured AlSi10Mg alloys, J. Alloys Compd. 945 (2023) 169315. https://doi.org/10.1016/j.jallcom.2023.169315.

[43] F. Trevisan, F. Calignano, M. Lorusso, J. Pakkanen, A. Aversa, E. Ambrosio, M. Lombardi, P. Fino, D. Manfredi, On the Selective Laser Melting (SLM) of the AlSi10Mg Alloy: Process, Microstructure, and Mechanical Properties, Materials 10 (2017) 76. https://doi.org/10.3390/ma10010076.

[44] A. Heidarzadeh, M. Khorshidi, R. Mohammadzadeh, R. Khajeh, M. Mofarrehi, M. Javidani, X.-G. Chen, Multipass Friction Stir Processing of Laser-Powder Bed Fusion AlSi10Mg: Microstructure and Mechanical Properties, Materials 16 (2023) 1559. https://doi.org/10.3390/ma16041559.

[45] İ.B. Toprak, N. Dogdu, Optimization of tensile strength of AlSi10Mg material in the powder bed fusion process using the Taguchi method, Sci. Rep. 14 (2024) 31172. https://doi.org/10.1038/s41598-024-82541-1.

[46] Y. Wu, B. Yan, Y. Han, J. Sun, M. Jiang, G. Zu, W. Zhu, X. Ran, High-temperature tensile properties of Cu-modified AlSi10Mg alloy fabricated by selective laser melting, J. Alloys Compd. 1001 (2024) 175190. https://doi.org/10.1016/j.jallcom.2024.175190.

[47] J. Mei, Y. Han, J. Sun, G. Zu, X. Song, W. Zhu, X. Ran, Achieving high strength in selective laser melting AlSi10Mg alloy by adding microsized pure Cu particles, Mater. Sci. Eng. A 880 (2023) 145357. https://doi.org/10.1016/j.msea.2023.145357.

[48] W. Pan, Z. Ye, Y. Zhang, Y. Liu, B. Liang, Z. Zhai, Research on Microstructure and Properties of AlSi10Mg Fabricated by Selective Laser Melting, Materials 15 (2022) 2528. https://doi.org/10.3390/ma15072528.

[49] K. Kempen, L. Thijs, J. Van Humbeeck, J.-P. Kruth, Mechanical Properties of AlSi10Mg Produced by Selective Laser Melting, Phys. Procedia 39 (2012) 439–446. https://doi.org/10.1016/j.phpro.2012.10.059.

[50] E. Sert, E. Schuch, A. Öchsner, L. Hitzler, E. Werner, M. Merkel, Tensile strength performance with determination of the Poisson's ratio of additively manufactured AlSi10Mg samples, Mater. Werkst. 50 (2019) 539–545. https://doi.org/10.1002/mawe.201800233.

[51] U. Gebhardt, T. Gustmann, L. Giebeler, F. Hirsch, J.K. Hufenbach, M. Kästner, Additively manufactured AlSi10Mg lattices – Potential and limits of modelling as-designed structures, Mater. Des. 220 (2022) 110796. https://doi.org/10.1016/j.matdes.2022.110796.

[52] J. Fiocchi, A. Tuissi, C.A. Biffi, Heat treatment of aluminium alloys produced by laser powder bed fusion: A review, Mater. Des. 204 (2021) 109651. https://doi.org/10.1016/j.matdes.2021.109651.

[53] R.E. Gite, V.D. Wakchaure, P.N. Nagare, Effect of annealing treatment on microstructure and mechanical behaviour of additively manufactured AlSi10Mg alloy, Prog. Addit. Manuf. 10 (2025) 4803–4817. https://doi.org/10.1007/s40964-024-00864-x.

7 Appendix

7.1 Fatigue testing specimen

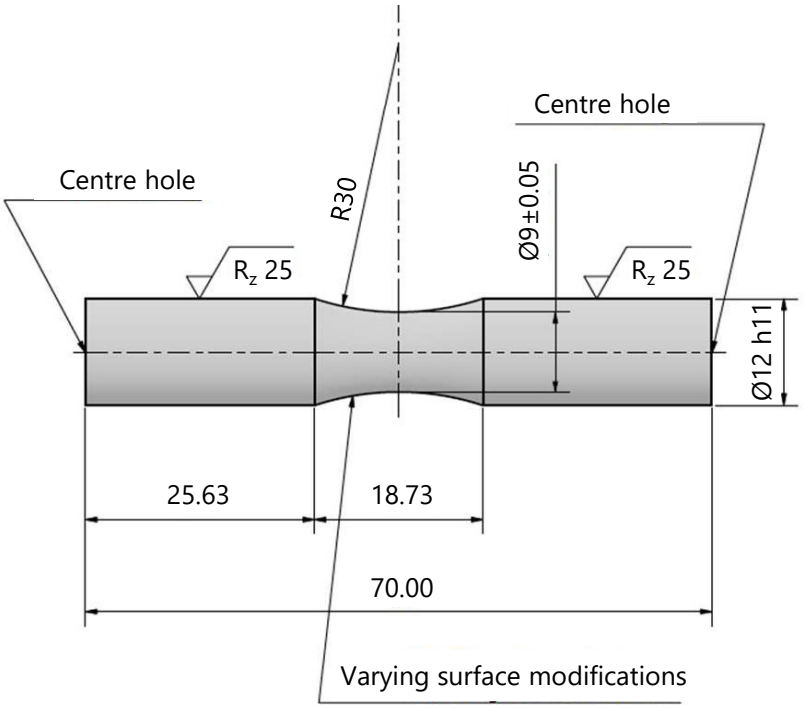

Figure A1 - Fatigue testing specimen. *Specimens featured a process "notch" with a large radius to concentrate highest stress during rotational bending into its the middle section. We chose this specimen geometry as it has a stress concentration factor $K_T > 1$. The shape should lead to locally confined stress states and reduces time-dependent deformation effects. Furthermore, the resulting stress gradient should minimise creep creep effects, which can be observed in cylindrical, unnotched specimens under loads near the yield strength (DIN 50100).*

7.2 Residual stress analyses

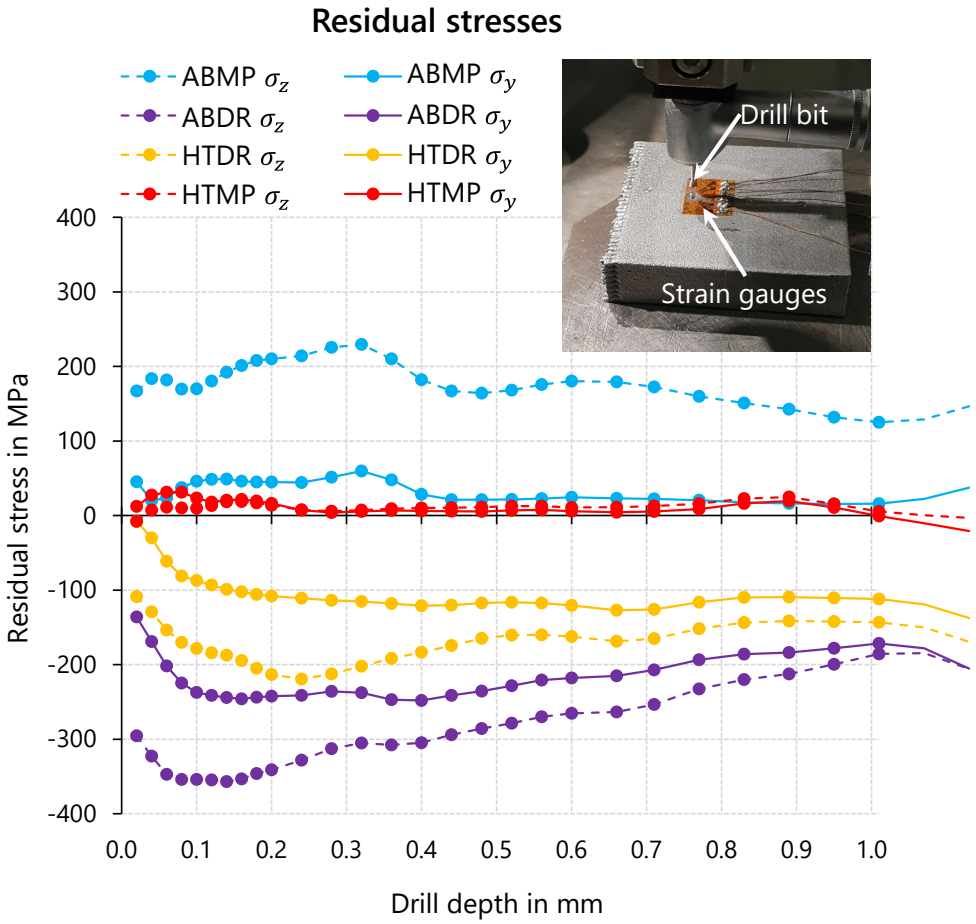

Figure A2 – Residual stresses in the as-built condition. *Residual stresses are shown for exemplary samples from the as built and manual polishing (ABMP), as built and heat treatment (HTMP), as built and deep rolling (ABDR), and heat treatment and deep rolling (HTDR) conditions. Residual stresses are higher in the built direction (σ_z) than in the direction perpendicular (σ_y) to it apart from the HTMP condition. ABMP is as close as possible to the as built (AB) condition and illustrates considerable tensile residual stresses. Heat treatment resolves stresses which explains the drop in the HTDR specimens. Plotting AB was not possible as the rough surface did not allow proper application of strain gauges. The inlay (top right) illustrates a test setup.*

7.3 Heat treatment and deep rolling.

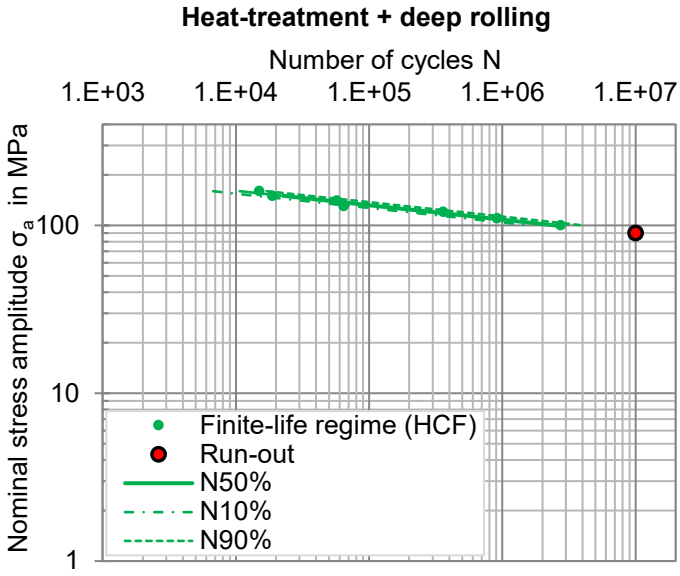

Figure A3 – Heat treatment and deep rolling: *(a) shows fatigue testing results as S–N curves including 10%, 50%, and 90% failure probabilities. the S–N curves are very flat while the run-out specimens are well below the level of the average. We observe that heat treatment counteracts the positive results of deep rolling as the slope of the compensation straight in this case is* $k = -11.63$ *in comparison to* $k = -23.94$ *when no heat treatment was involved. Nevertheless, the stress levels are higher than in the specimens without deep rolling.*

7.4 Magnified microscopy inlays

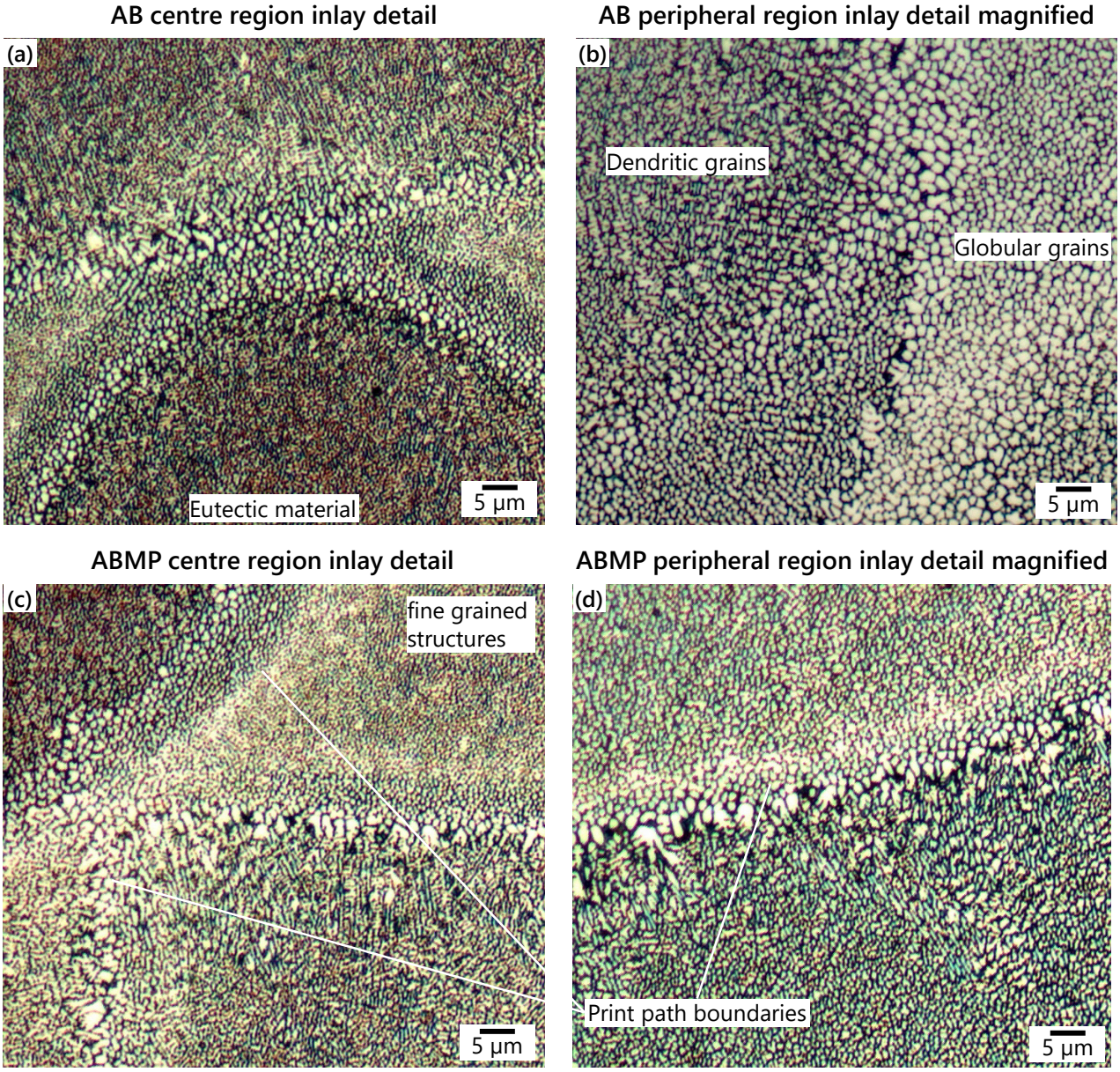

Figure A4 – Magnified metallography inlays for as-built (AB) condition: (a) shows a centre region and (b) a peripheral region in the AB condition. (c) and (d) show similar regions for AB with manual polishing (ABMP) samples. These specimens appear largely similar since the only difference in treatment is the polishing step. Within the print paths (Figure 4) in the centre region, dark regions dominate and indicate a silicon-rich eutectic network. The bright rims at the print path boundaries and at the outer specimen edge point to primary α-aluminium. This microstructural distribution arises from differing cooling conditions. The periphery and the boundary zones of the melt tracks cool particularly rapidly, which promotes the formation of globular α-aluminium and retains part of the silicon in solution. By contrast, slower cooling in the print path centres favours the development of a pronounced eutectic network.

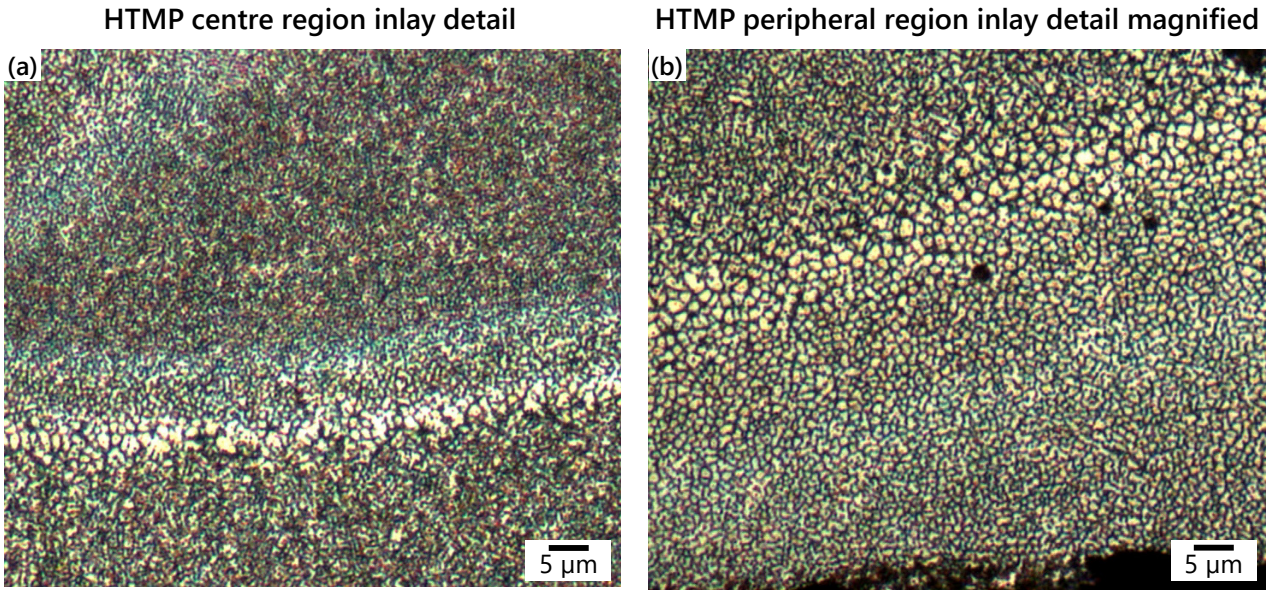

Figure A5 – Magnified metallography inlays for heat-treated samples with manual polishing (HTMP): (a) shows a centre region and (b) a peripheral region in the HTMP condition. These samples were etched with NaOH (Section 2.4) as Kroll was not working. After stress-relief annealing, the appearance changes markedly. The print path contours are faint, and phase contrast is reduced. Thermal relaxation causes silicon, previously supersaturated in the α-Al matrix, to precipitate finely during annealing, which modifies the original microstructure and leads to the formation of coarsened Si particles as well as Mg_2Si [32,33]. In the periphery (b) finer and more globular grains are visible and dendritic grains (Figure A4) disappear.

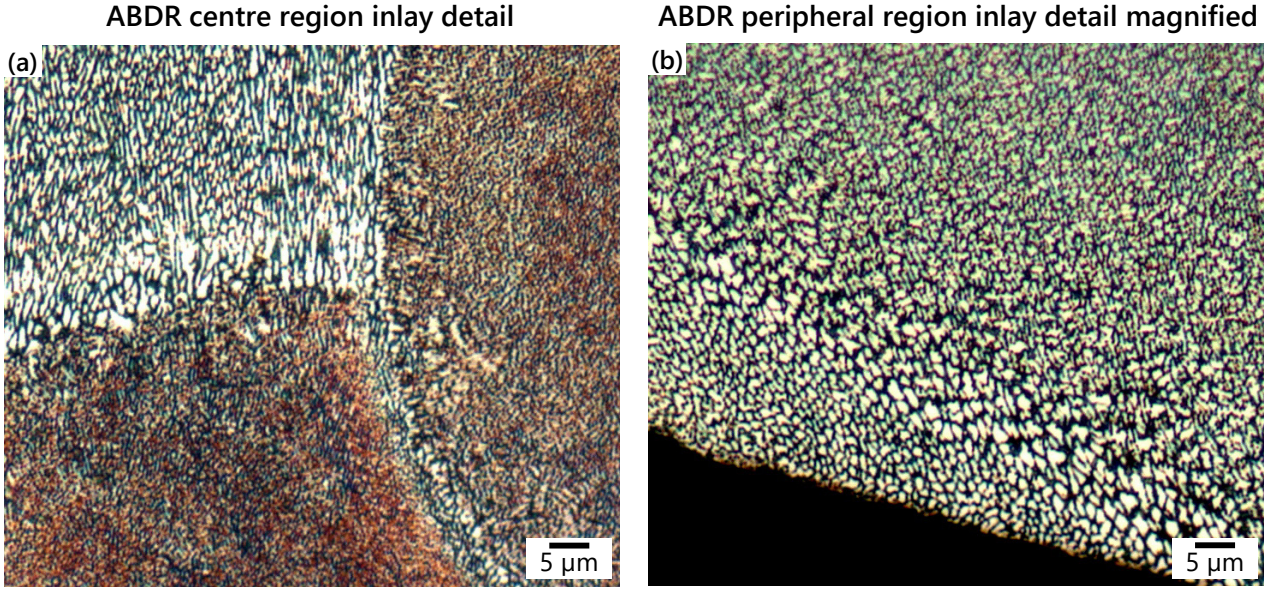

Figure A6 – Magnified metallography inlays for as-built + deep rolled (ABDR) samlpes: (a) shows a centre region and (b) a peripheral region in the ABDR condition. Appearance of ABDR samples from a metallographic perspective is largely similar to the as-built samples (Figure A4).